Mississippi State University
Scholars Junction

Theses and Dissertations | Theses and Dissertations

12-14-2018

The Effect of Two-Dimensional Wall Deformations on Hypersonic Boundary Layer Disturbances

Jeremy David Sawaya

Follow this and additional works at: https://scholarsjunction.msstate.edu/td

Recommended Citation

Sawaya, Jeremy David, "The Effect of Two-Dimensional Wall Deformations on Hypersonic Boundary Layer Disturbances" (2018). *Theses and Dissertations*. 4379.
https://scholarsjunction.msstate.edu/td/4379

This Graduate Thesis - Open Access is brought to you for free and open access by the Theses and Dissertations at Scholars Junction. It has been accepted for inclusion in Theses and Dissertations by an authorized administrator of Scholars Junction. For more information, please contact scholcomm@msstate.libanswers.com.

The effect of two-dimensional wall deformations on hypersonic boundary layer disturbances

By

Jeremy David Sawaya

A Thesis
Submitted to the Faculty of
Mississippi State University
in Partial Fulfillment of the Requirements
for the Degree of Master of Science
in Aerospace Engineering
in the Bagley College of Engineering

Mississippi State, Mississippi

December 2018

Copyright by

Jeremy David Sawaya

2018

The effect of two-dimensional wall deformations on hypersonic boundary layer disturbances

By

Jeremy David Sawaya

Approved:

_____

Adrian Sescu
(Major Professor)

_____

Davy M. Belk
(Committee Member)

_____

J. Mark Janus
(Committee Member)

_____

David S. Thompson
(Graduate Coordinator)

_____

Jason M. Keith
Dean
Bagley College of Engineering

Name: Jeremy David Sawaya

Date of Degree: December 14, 2018

Institution: Mississippi State University

Major Field: Aerospace Engineering

Major Professor: Adrian Sescu

Title of Study: The effect of two-dimensional wall deformations on hypersonic boundary layer disturbances

Pages in Study 67

Candidate for Degree of Master of Science

Previous experimental and numerical studies showed that two-dimensional roughness elements can stabilize disturbances inside a hypersonic boundary layer, and eventually delay the transition onset. The objective of the thesis is to evaluate the response of disturbances propagating inside a hypersonic boundary layer to various two-dimensional surface deformations of different shapes. The proposed deformations consist of a backward step, forward step, a combination of backward and forward steps, two types of wavy surfaces, surface dips or surface humps. Disturbances inside of a Mach 5.92 flat-plate boundary layer are excited by pulsed or periodic wall blowing and suction at an upstream location. The numerical tools consist of the Navier-Stokes equations in curvilinear coordinates and a linear stability analysis tool. Results show that all types of surface deformations are able to reduce the amplitude of boundary layer disturbances to a certain degree. The amount of reduction in the disturbance energy is related to the type of pressure gradient created by the deformation, adverse or favorable.

DEDICATION

I would like to dedicate this paper to my wife Kate Elizabeth Sawaya. She has been there since day one to challenge me and make sure I strive to do the very best that I can achieve. I want to also dedicate this paper to my parents and parent in laws for all their support through my years at Mississippi State.

ACKNOWLEDGEMENTS

Partial funding from the NASA EPSCoR RD Program MSGC, directed by Dr. Nathan Murray, is greatly acknowledged. I would like to acknowledge Dr. Sescu's guidance throughout my graduate school path to obtain my master's degree and creation of this thesis. I want to acknowledge and thank my fellow colleagues, especially Vasilis Sassanis and Sofia Yassir, for their assistance with performing the simulations. I want to also thank the committee for reviewing my thesis and providing suggestions for the thesis.

TABLE OF CONTENTS

DEDICATION ii

ACKNOWLEDGEMENTS iii

LIST OF TABLES v

LIST OF FIGURES vi

CHAPTER

I. INTRODUCTION 1

II. LITERATURE REVIEW 5

III. SIMULATION FORMULATION AND NUMERICAL ALGORITHM 10

Scalings 10
Governing Equations 11

IV. LINEAR STABILITY EQUATIONS 15

V. RESULTS AND DISCUSSIONS 18

Grid Convergence 20
Linear Stability Analysis 23
Variation in Wall Deformation Shape 25
Variation in Wall Deformation's Streamwise Extent 44
Variation of wall deformation height 55

VI. CONCLUSIONS 61

VII. FUTURE WORK 63

REFERENCES 64

LIST OF TABLES

1. Weights of the centered stencils 13

2. Flat Wall Grid Density.....20

LIST OF FIGURES

1 Time instance wall disturbance.....19

2 Pressure disturbance contours.....20

3 V-rms distribution for various grid resolutions. 22

4 Growth rates for different streamwise locations. 24

5 Linear stability analysis modes comparison. 24

6 Phase velocities for the slow and fast waves. 25

7 Computational grid meshes.....26

8 Mean pressure contours 29

9 Mean pressure distribution.....32

10 Pressure disturbance contours.....34

11 Time-averaged kinetic energy contours.....36

12 V-rms pulse disturbance in x-direction.....38

13 V-rms blowing and surction disturbance in x-direction 39

14 V-rms pulse disturbance in y-direction.....41

15 V-rms blowing and suction disturbance in y-direction.....42

16 P-rms of blowing and suction disturbance in y-direction 43

17 Backward-forward streamwise meshes.....45

18 backward-forward streamwise width distribution plots.....45

19 Forward-backward streamwise meshes 46

20 Forward-backward streamwise distribution plots.....47

21 Surface hump streamwise meshes 48

22 Surface hump streamwise distribution plots 49

23 Surface dip streamwise meshes 50

24 Surface dip streamwise distribution plots 51

25 Wavy surface (sine 1) streamwise meshes.....52

26 Wavy surface (sine1) streamwise distribution plots 53

27 Wavy surface (sine 2) streamwise meshes.....54

28 Wavy surface (sine 2) distribution plots 55

29 Variation in discontinuous deformation heights 56

30 Variation in continuous deformation heights.....59

CHAPTER I

INTRODUCTION

Surface imperfections play a vital role as disturbing factors in boundary layer transition, and it is noticed in experiments (Gregory et al.[1], Drake et al.[2], Duncan et al.[3]) and numerical simulations (Choudhari and Fischer[4], Yoon et al.[5], Muppidi and Mahesh[6], Iyer et al.[7], Brehm et al.[8], Duan and Choudhari[9], Subbareddy et al.[10], Rizzetta and Visbal[11], Sescu et al.[12,13], Chaudhry et al.[14]) that they can have a significant impact on the boundary layer receptivity and transition. Direct numerical simulations showed that small steps may impact the transition onset, depending on the type and height of the step, as well as the flow conditions.

The interest in analyzing the effects of surface imperfections on the transition in supersonic and hypersonic boundary layers has been revisited in recent years. The transition at supersonic speeds is sensitive to the shape and height of the surface imperfections and the Reynolds number. The transition is also dependent on the Mach number, freestream temperature, thermal boundary conditions at the wall and shock waves that may develop from the presence of surface imperfections. The way shock waves impact the transition in high-speed boundary layer flow is still unclear. Many of the studies involving surface imperfections looked into isolating roughness elements of different shapes and heights (Fong et al.[15-18], Duan et al.[19], Park and Park[20], Bountin et

al.[21], Mortensen and Zhong[22]). A comprehensive review of the effect of different roughness elements on hypersonic boundary layers can be reviewed in Schneider[23].

Acoustic waves were found to be very effective in exciting high-speed boundary layers because the phase speed of the acoustic waves synchronize with the phase speed of the first modes that correspond to the lower branch of the neutral stability curve. There are numerous studies involving the interaction of acoustic waves with supersonic boundary layers (Mack[24], Gaponov[25], Gaponov and Smorodsky[26], Fedorov and Khokhlov[27,28], Sakaue et al.[29], Fedorov[30]). In some of the studies, it was found that the acoustic waves are very effective in exciting disturbances inside the boundary layer with amplitudes that become much larger than those in the freestream, but this happens only above some critical Reynolds number as in the incompressible regime. Other studies (Fedorov and Khokhlov[27,28], Sakaue et al.[29], Fedorov[30]) were concerned about the generation of the first and second modes in the vicinity of the leading edge. The effect of all types of waves, i.e. slow and fast acoustic waves, vorticity waves and entropy waves, on supersonic boundary layers were studied and reported in a suite of papers by Balakumar[31-33]. The generation and evolution of three-dimensional disturbanes induced by slow and fast acoustic disturbances and isolated roughness elements in a supersonic boundary layer over a flat plate and wedges were numerically investigated by solving the full three-dimensional Navier-Stokes equations. It was discovered that the instability waves are generated within one wavelength of the acoustic wave from the leading edge (Sawaya et al.[43]).

In previous experimental and numerical studies (Holloway and Sterret[34], Fong et al.[15-18], Duan et al.[19], Park and Park[20], Mortensen and Zhong[22]) showed evidence that

two-dimensional roughness elements can reduce the amplitude of disturbances inside high-speed boundary layers. Holloway and Sterret[34] carried out early experiments on flat plate boundary layer being disturbed by roughness elements, with a freestream Mach number of 4.0 and 6.0. They observed a delay in the transition for roughness elements with a height smaller than the local boundary layer thickness. Duan et al.[19] and Fong et al.[15-18] investigated the effects of two-dimensional roughness on the instability of the second mode, or mode S, with direct numerical simulations (DNS). Their numerical results proved that the roughness located downstream of the synchronization point could stabilize the second mode. Park and Park[20] studied the effect of a two-dimensional smooth hump on linear instability of hypersonic boundary layer by using parabolized stability equations. Their results confirmed the findings of the previous studies, that the mode S is stabilized by the hump when it is in the downstream of the synchronization point. But, they also found that this mode is destabilized when the hump is located upstream of the synchronization point. Experimental and computational work by Bountin et al.[21] showed that a wavy surface led to a considerable reduction in the spectral peak associated with the second mode instability inside a Mach 6 boundary layer.

Previous studies have focused on localized disturbances propagating as wave packets inside of the boundary layer. In this study, the effect of 2D surface deformations on pulsed and periodic disturbances propagating inside a high-speed boundary layer will be analyzed. The wall deformations being studied here are: backward or forward steps, combinations of backward and forward steps, surface dips, surface humps and wavy surfaces with the mean above or below the wall surface. The numerical tool utilized is a high-accurate solver, discretizing the unsteady, compressible, conservative form of the

Navier-Stokes equations written in body-fitted curvilinear coordinates. Velocity and temperature profiles corresponding to a compressible boundary layer are imposed at the inflow, thus avoiding the inclusion of the leading edge shock in the computation. Due to the study being 2D, there are limitations on the types of modes being considered: for example, in the 2D framework only the second mode is predominant, while the oblique first mode is not captured by the analysis. From the results, it is noticed that all types of wall deformations can reduce the amplitude of the boundary layer disturbances to a certain degree. It is suggested that the oblique Mach wave that is posed by the wall deformations is responsible for deviating a small portion of the kinetic energy of the disturbance to the external flow. This may be a potential cause for disturbance energy reduction in the downstream of the roughness element. The type of pressure gradient that is posed first by the surface deformation is also a factor in the reduction of the disturbance energy, among other factors, such as the location of the synchronization point with respect to the disturbance energy, and the location of the synchronization point with respect to the location of the roughness element.

In Chapter II, literary research is performed on previous studies focusing on the effects of roughness elements on high-speed boundary layer flow. In Chapter III, the scaling, governing equations and numerical tool utilized for the study are introduced and described. In Chapter IV, the linear stability analysis methodology is described. In Chapter V, the results from the study are displayed in qualitative and quantitative plots and discussed, while Chapter VI is reserved for conclusions and future work.

CHAPTER II

LITERATURE REVIEW

In Fong et al.[16], the influence of a single roughness element on the stability of the flat plate hypersonic boundary layer is investigated. The roughness element described in the paper resembles a semi-circle on the surface of the flat plate. Four cases were simulated to obtain the results, with four different roughness element heights per test case. The roughness element height was chosen to be a fraction of the boundary layer thickness (δ). The four element heights used in the four test cases were 0.25δ, 0.375δ, 0.5δ and 0.625δ. The first test case (x_r = 0.1101 m) involved locating the roughness element approximately 0.2209 m upstream of the synchronization point (the synchronization point is defined as the location where the phase speeds of the fast mode F and slow mode S become equal). The roughness element in the second test case (x_r = 0.185 m) was approximately 0.146 m upstream of the synchronization point. In the third test case (x_r = 0.331 m), the roughness element is located at the synchronization point. For the fourth test case (x_r = 0.410 m), the roughness element is approximately 0.079 m downstream of the synchronization point.

In order to obtain the location of the synchronization point for the flat plate case, Fong utilized the multi-domain LST spectral method reported in Malik et al[35]. After performing the linearized stability analysis on the flat plate with no roughness element

present, the synchronization point was located a 0.331 m. The effect of the roughness element on the Mode S perturbation was primarily analyzed and displayed. For case 1 and case 2, the roughness element was placed upstream of the synchronization point, which resulted in an amplification of the perturbations present in the simulation when there was no roughness element present. As the height of the roughness element increased, the amplification factor of the perturbation increased drastically. For case 3, the roughness element was placed at the location of the synchronization point. During this test case, the height of the roughness element had a very distinct effect on the perturbations of the test case. When the height of the roughness element was 0.25δ, the perturbations continue to grow in the downstream as if there was no roughness element present. But, when the height of the roughness element was greater than 0.25δ, a damping of the perturbations downstream of the roughness element and right before the element became prevalent. For test case 4, where the roughness element was located downstream of the synchronization point, the perturbations were dampened by each test height of the roughness element. As the roughness element height was increased, the greater reduction in the perturbations was present. Based on the results from the four test cases that Fong executed, placing a roughness element downstream of the synchronization point for the imposed mode can act as an efficient dampener and could potentially stabilize a flow.

In Zhou et al.[36], simulations were conducted to analyze the influence of a wavy surface on the transition and stability of the hypersonic boundary layer. The wavy surface was created with the following equations:

$$y(x) = \begin{cases} \sqrt{R^2 - (x - x_m + l/2)^2}, & -R, x_s < x < x_m \\ \sqrt{R^2 - (x - x_m + l/2)^2}, & -R, x_m < x < x_e \end{cases}$$

where $l = 12mm, h = 1.8mm, R = \frac{h}{2} + \frac{l^2}{8h}, x_m = \frac{x_s + x_e}{2}$ (Zhou et al.[36]). The free-stream conditions were defined as: $M_\infty = 6, Re_\infty = 10.5 \times 10^6, T_\infty = 43.18K$. Zhou introduced a periodic disturbance into the simulated flow by periodic blowing and suction. In the paper, Zhou performed three simulation cases with the wavy wall surface, where the wave number was altered, the wall depth was altered, then the streamwise location of the wavy wall surface was analyzed.

The first set of simulations involved testing five different wavy wall wave numbers. The wave numbers utilized were 1, 3, 6, 9 and 12, with the depth of the wavy wall set to 1.8mm and the starting location of the wavy wall at 52mm. The wave number reveals how many times the disturbance of the wavy wall is modulated, thus showing the effect of how various identical disturbances alter the stability of the hypersonic flow. For the case when n=1, the disturbance from the wavy wall initially caused the amplitude of the second-mode to reduce as compared to the flat plate case, but then the pressure coefficient returned to the amplitude corresponding to the flat plate case, approximately 90mm downstream of the beginning of the wavy wall. Then, the amplitude of the pressure coefficient reaches a maximum value above the maximum value achieved in the flat plate case. For the rest of the cases, where n=3,6,9,12, the maximum amplitude of the pressure coefficient does not reach the maximum amplitude of the flat plate case. The n=12 case greatly reduced the pressure coefficient amplitude downstream of the wavy wall, by a reduction of almost half when compared to the flat plate case.

For the second round of simulations, the starting location of the wavy wall is 52mm, the number of disturbance modulations is 9, and the depth of the wavy wall is analyzed at three different depths: 1.8mm, 2.1mm, 2.4mm. From the plots, one can notice that as the depth of the wavy wall disturbance increases, the amplitude of the pressure coefficient has a noticeable reduction downstream of the disturbance. The reduction of the pressure coefficient from the wavy wall depth of 2.4mm is almost identical to the pressure coefficient reduction of the wavy wall when the disturbance is modulated by 12 with a depth of 1.8mm.

For the last set of simulations, the wavy wall disturbance modulations is set to 9, the wavy wall depth is equal to 1.8mm and three starting wavy wall locations are analyzed in this set of simulations: 32mm, 52mm, 72mm. When the wavy wall begins at 32mm, the pressure coefficient is slightly reduced, while the greatest reduction of the pressure coefficient was from the wavy wall beginning at 72mm. The overall reduction of the pressure coefficient is close to the overall reduction from the wavy wall with the disturbance modulation equal to 12. The reduction of the pressure coefficient when the wavy wall begins at 72mm could be from the wavy wall beginning downstream of the synchronization point of the fast and slow acoustic wave, while the wavy wall for the 32mm case is upstream of the synchronization point.

Based on the results of the simulations performed by Zhou, pertaining to the influence of a wavy wall to a hypersonic boundary layer, changing the position of where the wavy wall disturbance begins has the greatest reduction on the pressure coefficient. The reduction in the pressure coefficient helps proves that the transition of the hypersonic flow from laminar to turbulent is delayed to farther downstream.

In Park and Park[20], the study focused on the effect of a two-dimensional smooth hump on the instability of a hypersonic boundary layer with the assistance of parabolized stability equations. The three main cases that were analyzed involved the smooth hump in a Mach 4.5 and 5.92 boundary layer flow over a flat plate and a Mach 7.1 flow in a sharp cone boundary layer. The effect of the surface hump's location with respect to the synchronization point was analyzed by plotting the N-factor curves of F=50 (frequency) when the hump was placed upstream of the synchronization point and then downstream of the synchronization point. Based on Figure 11 in Park and Park[20], when the surface hump was located upstream of the synchronization point, the curves had a higher N-factor than the flat wall case, but as the location of surface moves downstream of the synchronization point, the N-factor becomes lower than the flat wall case. When the surface hump was located at L = 1.6m, approximately 0.15m downstream of the synchronization point, the hump had the greatest stabilization effect on the mode S in the hypersonic boundary layer. The results for the 5.92 Mach speed boundary layer case, exhibited similar results as the previous described above. Based on these results from Park and Park[20], when there is a roughness element present downstream of the synchronization point of the acoustic waves, then the transition to turbulent flow is able to be delayed within the high-speed boundary layer.

CHAPTER III

SIMULATION FORMULATION AND NUMERICAL ALGORITHM

Scalings

The governing equations employed for the numerical simulations are the full Navier-Stokes equations written in generalized curvilinear coordinates, where the spatial coordinates in the computational space are expressed in terms of the spatial coordinates in the physical space as $\xi = \xi(x, y)$, $\eta = \eta(x, y)$, where ξ and η are the spatial coordinates in the computational space, with *x* and *y* as the spatial coordinates in the physical space. The transformation allows for seamless mapping of the solution of the computational to the physical space and vice versa. All dimensional spatial coordinates are normalized by the boundary layer thickness at the inflow, δ^*,

$$(x, y) = \frac{(x^*, y^*)}{\delta^*} \tag{1}$$

the velocity is scaled by the freestream velocity magnitude V_∞^*,

$$(u, v) = \frac{(u^*, v^*)}{V_\infty^*} \tag{2}$$

The pressure is scaled by the dynamic pressure at infinity, $\rho_\infty^* {V_\infty^*}^2$, and the temperature by the freestream temperature, T_∞^*. The Reynolds number based on the boundary layer thickness, Mach number and Prandtl number are defined as

$$Re_\lambda = \frac{\rho_\infty^* V_\infty^* \delta^*}{\mu_\infty^*}, \quad M = \frac{V_\infty^*}{a_\infty^*}, \quad Pr = \frac{\mu_\infty^* C_p}{k_\infty^*} \tag{3}$$

where μ_∞^*, a_∞^* and k_∞^* are freestream dynamic viscosity, speed of sound and thermal conductivity, respectively; and C_p is the specific heat at constant pressure. All simulations are performed for air as an ideal gas (Sawaya et al.[43]).

Governing Equations

A hypersonic flat-plate boundary layer is considered with small two-dimensional surface non-uniformity located at a certain distance from the leading edge. In the conservative form, the Navier-Stokes equations are written as

$$\boldsymbol{Q}_t + \boldsymbol{F}_\xi + \boldsymbol{G}_\eta = \boldsymbol{S}, \tag{4}$$

where the conservative variable vector is

$$\boldsymbol{Q} = \frac{1}{J}\{\rho,\ \rho u_i,\ E\}^T, i = 1,2 \tag{5}$$

and ρ is density of the fluid, $u_i = (u, v)$ is the physical space velocity vector, and E is the total energy. The flux vectors **F** and **G**, are defined as,

$$\boldsymbol{F} = \frac{1}{J}\left\{\rho U,\ \rho u_i U + \xi_{x_i}\left(p + \tau_{i_1}\right),\ EU + p\tilde{U} + \xi_{x_i}\Theta_i\right\}^T \tag{6}$$

$$\boldsymbol{G} = \frac{1}{J}\left\{\rho V,\ \rho u_i V + \eta_{x_i}\left(p + \tau_{i_2}\right),\ EV + p\tilde{V} + \eta_{x_i}\Theta_i\right\}^T \tag{7}$$

where the contravariant velocity components are given by

$$U = \xi_{x_i} u_i,\ V = \eta_{x_i} u_i \tag{8}$$

with the Einstein summation convention applied over i, j. The shear stress tensor and the heat flux are given as

$$\tau_{ij} = \frac{\mu}{Re}\left[\left(\frac{\partial \xi_k}{\partial x_j}\frac{\partial u_i}{\partial \xi_k} + \frac{\partial \xi_k}{\partial x_i}\frac{\partial u_j}{\partial \xi_k}\right) - \frac{2}{3}\delta_{ij}\frac{\partial \xi_l}{\partial x_k}\frac{\partial u_k}{\partial \xi_l}\right] \tag{9}$$

$$\Theta_i = u_j \tau_{ij} + \frac{\mu}{(\gamma-1)M_\infty^2 RePr}\frac{\partial \xi_l}{\partial x_i}\frac{\partial T}{\partial \xi_l} \tag{10}$$

and **S** is the source vector term. The pressure p, the temperature T and the density of the fluid are combined in the equation of state, $p = \rho T/\gamma M_\infty^2$ when non-reacting flows are considered. The Jacobian of the curvilinear transformation from the physical space to the computational space is denoted by J. The derivatives ξ_x, ξ_y, η_x, η_y represent the grid metrics. The variables are non-dimensionalized by their respective free-stream variables, except with pressure being non-dimensionalized by ρV_∞. The dynamic viscosity and the thermal conductivity are linked to the temperature by Sutherland's equations in dimensionless form,

$$\mu = T^{3/2}\frac{1+C_1/T_\infty}{T+C_1/T_\infty}; \quad k = T^{3/2}\frac{1+C_2/T_\infty}{T+C_2/T_\infty} \tag{11}$$

where air at sea level, $C_1 = 110.4K, C_2 = 194K$ and T_∞ is a reference temperature.

A high-order numerical algorithm is employed to solve the Navier-Stokes equations, where the time integration is performed using a third order TVD Runge-Kutta method (Liu et al.[37]) written in the form

$$\begin{aligned} \boldsymbol{Q}^0 &= \boldsymbol{Q}^n \\ \boldsymbol{Q}^1 &= \boldsymbol{Q}^0 + \Delta t L(u^0) \\ \boldsymbol{Q}^2 &= \tfrac{3}{4}\boldsymbol{Q}^0 + \tfrac{1}{4}\boldsymbol{Q}^1 + \tfrac{1}{4}\Delta t L(\boldsymbol{Q}^1) \\ \boldsymbol{Q}^{n+1} &= \tfrac{1}{3}\boldsymbol{Q}^0 + \tfrac{2}{3}\boldsymbol{Q}^1 + \tfrac{2}{3}\Delta t L(\boldsymbol{Q}^2) \end{aligned} \tag{12}$$

where $L(\mathbf{Q})$ is the residual and Δt is the time step; while the spatial derivatives are discretized using either a dispersion relation preserving scheme (Tam and Webb[38]) or a high resolution 9-point dispersion relation preserving optimized scheme (Bogey et al[39]). The spatial discretization scheme can be written as $(\partial_x f)_l \simeq 1/\Delta x \sum_{j=-N}^{M} a_j f_{l+j}$ where the coefficients are given in Table 1.

Table 1. Weights of the centered stencils

Stencil	$a_1 = -a_{-1}$	$a_2 = -a_{-2}$	$a_3 = -a_{-3}$	$a_4 = -a_{-4}$
DRP	0.77088238	-0.16670590	0.02084314	0
FDo9p	0.84157012	-0.24467863	0.05946358	-0.00765090

To damp out the unwanted high wavenumber waves from the solution, high order spatial filters, developed by Kennedy and Carpenter[40], are applied to all variables. Nonreflecting boundary conditions (Kim and Lee[41]) are used at the inflow boundary and extrapolation at the outflow boundary. The mean inflow conditions, consisting of velocity, density and temperature profiles, are obtained separately from a precursor two-dimensional simulation, where a Blasius type boundary condition is imposed in the upstream. A 'slice' of data from the two-dimensional flow domain is imposed at the inflow boundary of the main domain.

No slip boundary conditions for velocity and isothermal condition for temperature are imposed at the solid surface. Sponge layers are imposed in the proximity of the far-field boundaries, and combined with grid stretching to damp out the unwanted spurious waves; these sponge layers are set outside the flow domain since they generate unphysical solutions (Sescu et al.[12]). The shock capturing techniques are necessary to avoid unwanted oscillations that may propagate from potential discontinuities. In this study, we apply a shock capturing methodology that was proven to work efficiently for high-order, nonlinear computations (Bogey et al.[42]). In present work high-order, central-difference schemes are used to achieve increased resolution of the propagating disturbances, a straightforward approach is a model which introduces sufficient numerical viscosity in

the area of the discontinuities, and negligible artificial viscosity in the rest of the domain. A shock-capturing technique, suitable for simulations involving central difference in space is applied, based on the general explicit filtering framework. The technique introduces selective filtering at each grid vertex to minimize numerical oscillations, and shock-capturing in the areas where discontinuities are present (refer to Bogey et al.[42] detailed information). (Sawaya et al.[43])

CHAPTER IV

LINEAR STABILITY EQUATIONS

For the two-dimensional Cartesian coordinate system, x and y are defined as the streamwise and wall-normal direction respectively. The velocity components are scaled by the reference velocity V_∞, the spatial coordinates by the boundary layer thickness δ, density by ρ_∞, pressure by $\rho_\infty V_\infty^2$, time by δ/V_∞ and other variables are scaled by the corresponding boundary layer edge components (Malik et al.[35]). Once the components have been properly scaled, the instantaneous values for velocity (*u, v*), pressure (*p*), temperature (τ), density (ρ), dynamic viscosity (μ) and thermal conductivity coefficient (k) are represented as a summation of the mean and the disturbance quantity,

$$u = \bar{U} + \tilde{u}, v = \bar{V} + \tilde{v}, p = \bar{P} + \tilde{p}, \tau = \bar{T} + \tilde{T}, \rho = \bar{\rho} + \tilde{\rho}, \mu = \bar{\mu} + \tilde{\mu}, k = \bar{k} + \tilde{k}. \quad (13)$$

For the local compressible boundary layer flow, the "locally parallel flow" assumption in the Orr-Sommerfield equation for incompressible flow is utilized. With the locally parallel flow assumption, the mean quantities are a function of the wall-normal coordinate only,

$$U = U(y),\ V = V(y), T = T(y),\ \rho = \rho(y) \quad (14)$$

with *P* assumed to be constant across the boundary layer and equal to $1/\rho M^2$, and $\rho = 1/T$. As a result, the density disturbance ($\tilde{\rho}$) becomes,

$$\tilde{\rho} = \gamma M^2 \frac{\tilde{p}}{T} - \frac{\tilde{T}}{T^2}. \quad (15)$$

With the newly defined equation for $\tilde{\rho}$ and the Sutherland equations, the equations for $\tilde{\mu}$ and $\tilde{k}$ are derived to become,

$$\tilde{\mu} = \frac{d\mu}{dT}\tilde{T}, \tilde{k} = \frac{dk}{dT}\tilde{T}. \tag{16}$$

To derive the stability equations, the fluctuations in velocity, pressure and temperature are assumed to resemble a harmonic wave defined as

$$[\tilde{u}, \tilde{v}] = [\hat{u}(y), \hat{v}(y)]e^{i(\alpha x - \omega t)} \tag{17}$$

$$\tilde{p} = \hat{p}(y)e^{i(\alpha x - \omega t)} \tag{18}$$

$$\tilde{T} = \hat{T}(y)e^{i(\alpha x - \omega t)} \tag{19}$$

where α is the wavenumber and ω is the frequency where the velocity, pressure and temperature are complex. Based on the spatial stability theory, the frequency ω is considered real, while the wavenumber α is a complex number to be determined. For the temporal stability theory, the wavenumber α is considered real, and the frequency ω is the complex unknown. The Navier-Stokes equations are first linearized around the mean flow, resulting in a set of equations for disturbances. Then, equations (17)-(19) are plugged into the disturbance equations to obtain the following system of ordinary differential equations, which form an eigenvalue problem,

$$(AD^2 + BD + C)\Phi = 0, \tag{20}$$

where Φ is a four-element vector defined as

$$\{\hat{u}, \hat{v}, \hat{p}, \hat{T}\}^{tr}. \tag{21}$$

A is a four by four matrix defined as

$$A = \begin{bmatrix} 1 & 0 & 0 & 0 \\ 0 & 1 & 0 & 0 \\ 0 & 0 & 0 & 0 \\ 0 & 0 & 0 & 1 \end{bmatrix} \tag{22}$$

The four by four matrices for B and C are given in Appendix I of Malik et al.[35], and $D \equiv \frac{d}{dy}$. The boundary conditions associated with homogeneous differential equation (20) are

$$y = 0;\ \phi_1 = \phi_2 = \phi_4 = 0 \tag{23}$$

$$y \to \infty;\ \ \phi_1, \phi_2, \phi_4 \to 0. \tag{24}$$

The wall is treated as an insulated wall for the temperature variable of the mean flow, while the temperature perturbations are zero for the solid boundary wall. When the disturbance frequency is high, this assumption becomes acceptable. The temperature perturbations are unable to penetrate the solid wall, due to the thermal inertia of the solid wall. When temporal stability analysis is assumed, equation (20) is discretized with the use of finite difference schemes normal to the wall normal direction, resulting with the eigenvalue problem

$$E\Phi = \omega F\Phi \tag{25}$$

is obtained, where E and F are four by four matrices from A, B and C. The boundary layer coordinate y, $0 \le y \le y_{max}$, is mapped into the computational domain, $0 \le \eta \le 1$, with the use of algebraic mapping

$$y = \frac{a\eta}{b-\eta}, where\ b = 1 + \frac{a}{y_{max}}\ .$$

The term y_{max} is where the free-stream boundary conditions are satisfied and a is the chosen scaling parameter to optimize the accuracy of calculations. The scaling parameter is set to $a = y_{max}\, y_i/(y_{max} - 2y_i)$, this results in half of the node points being located between $y = 0$ and $y = y_i$ for discretization. The eigenvalue problem presented by equation (25) is then solved with LR or QR methods (Malik et al.[35]).

CHAPTER V

RESULTS AND DISCUSSIONS

The flow domain of the simulations utilized for the results were a flat-plate boundary layer with the freestream flow traveling at M = 5.92. The x-axis is lined up with the surface of the flat-plate, and the y-axis is set up normal to the surface of the flat-plate. The dimensions of the grid domain is 50 mm tall and 600 mm long. The Reynolds number based on the boundary layer thickness, and the freestream velocity is 22,750. Due to the physical frequency of the disturbances set to 132 kHz, the non-dimensional angular frequency is equal to 0.5 for the simulation disturbances. The wall has a constant temperature equal to $T_w = 48.69\ K$, which is equal to the ambient temperature.

The grid mesh for the simulations has approximately 650,000 grid points, with the necessary grid resolution near the wall and proper locations close to the wall deformations described in section 3 of the results. The spatial coordinates are nondimensionalized by the height of the wall deformation. The velocity, density and temperature are nondimensionalized by the freestream velocity, density and temperature respectively, and the pressure is nondimensionalized by the dynamic pressure of the freestream flow.

There are two types of disturbances that will be imposed from the wall with the wall normal velocity defined as

$$v_w(x,t) = A \sin\left[\pi \frac{(x-x_1)}{(x_2-x_1)}\right]^2 \sin(\omega t), \tag{26}$$

where A is the amplitude of the wave, x_1 and x_2 are the start and end points along the streamwise direction for the wall disturbance, and ω is the angular frequency. For the simulations presented in this thesis, $x_1 = 50$ and $x_2 = 57$, and the inflow boundary is located at the beginning of the flow domain, which is set at $x = 0$. The disturbance for different time instances are plotted together in Figure 1. The first type of disturbance that will be utilized in the simulations is a pulse disturbance at time interval $[0, 2\pi/\omega]$, which generates a localized pulse that travels downstream with the mean flow. As a result, the wave will grow and/or decay as it propagates downstream in the flow domain, dependent on the boundary layer conditions and the amplitude of the pulse. The second disturbance that will be utilized in the simulations is periodic oscillations that begin at x_1 and will be analyzed within the boundary layer (for the periodic oscillations disturbance, the wall transpiration disturbance if imposed continuously in the time interval [0,∞)) (Sawaya et al).

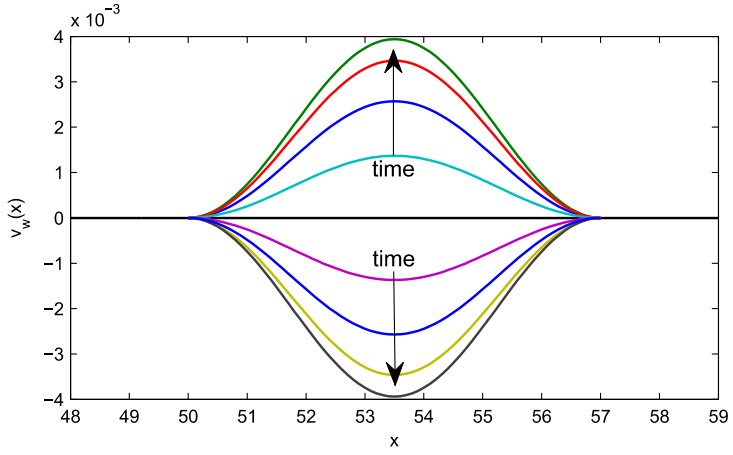

Figure 1 Wall disturbance imposed between $x = 50$ and $x = 57$.

Grid Convergence

This section will analyze the influence of grid resolution on the computational accuracy of the results for the flat wall case. The five different grid density cases are listed below in Table 2.

Table 2. Flat Wall Grid Density

Case	Horizontal Density	Vertical Density
g0	900	180
g1	1080	240
g2	1440	300
g3	1800	360
g4	2160	420

The grid density case g0 has the coarsest grid of 900 x 180, while grid density case g4 has the finest grid of 2160 x 420. Figure 2 displays the pressure contour plots of the five grid density cases for the smooth case when the wall disturbance is a periodic blowing-suction disturbance.

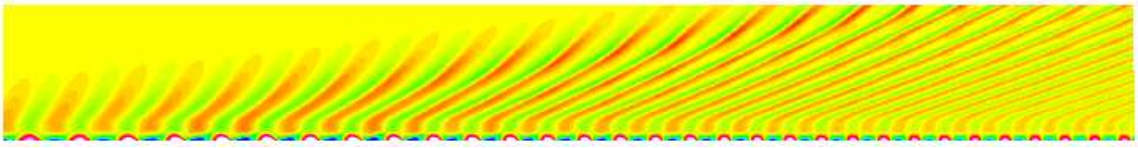

Figure 2 Pressure disturbance contours

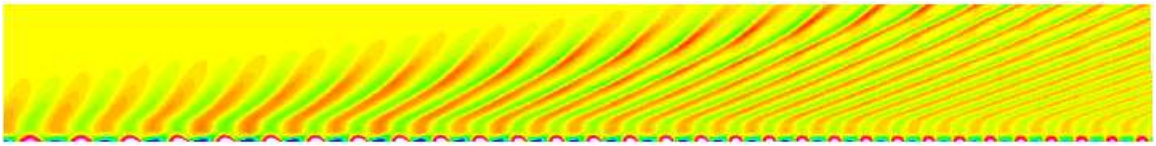

Figure 2b)

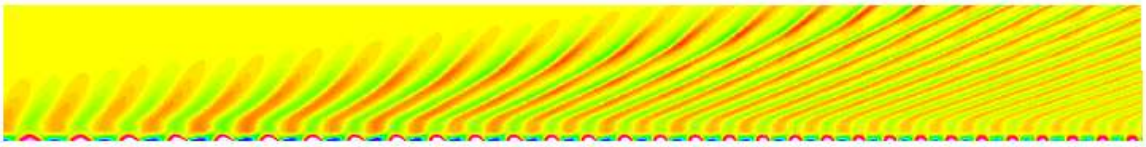

Figure 2c)

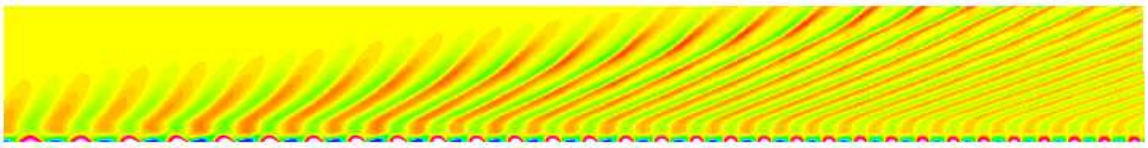

Figure 2d)

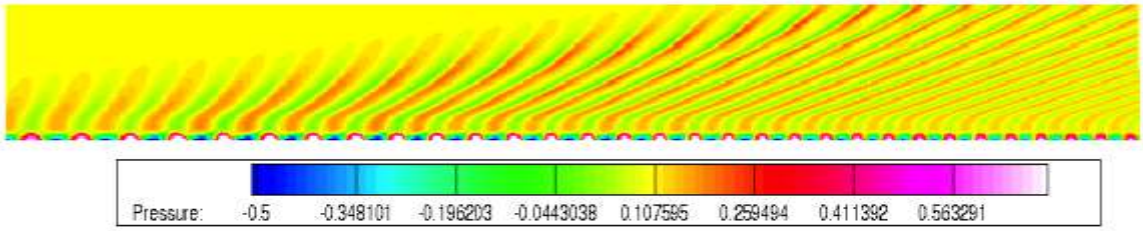

Figure 2e)

Pressure disturbance contours for a) g0, b) g1, c) g2, d) g3 and e) g4 grid cases of different grid densities.

The root-mean square (rms) velocity normal to the wall for the five cases is plotted in Figure 3 on a semi-log scale. The semi-log scale is utilized to analyze the convergence rates among the five grid density cases to determine which one provides the most accurate and computational efficient grid density for the upcoming computational simulations. The root mean square was calculated as

$$v'_{rms}(x,y) = \sqrt{\frac{1}{T}\int_t^{t+T}[v'(x,y,t)]^2 dt} \tag{27}$$

where the time span T was in order of the time it takes a disturbance to go from the inlet boundary to the outlet boundary.

From Figure 3, it can be noted that case g3 and g4 has almost identical root mean square distribution, while the root mean square distribution of g0 and g1 are the least converged with each other. Based on these results, the grid density for case g3 (1800 x 360) is selected for the the other wall deformation cases.

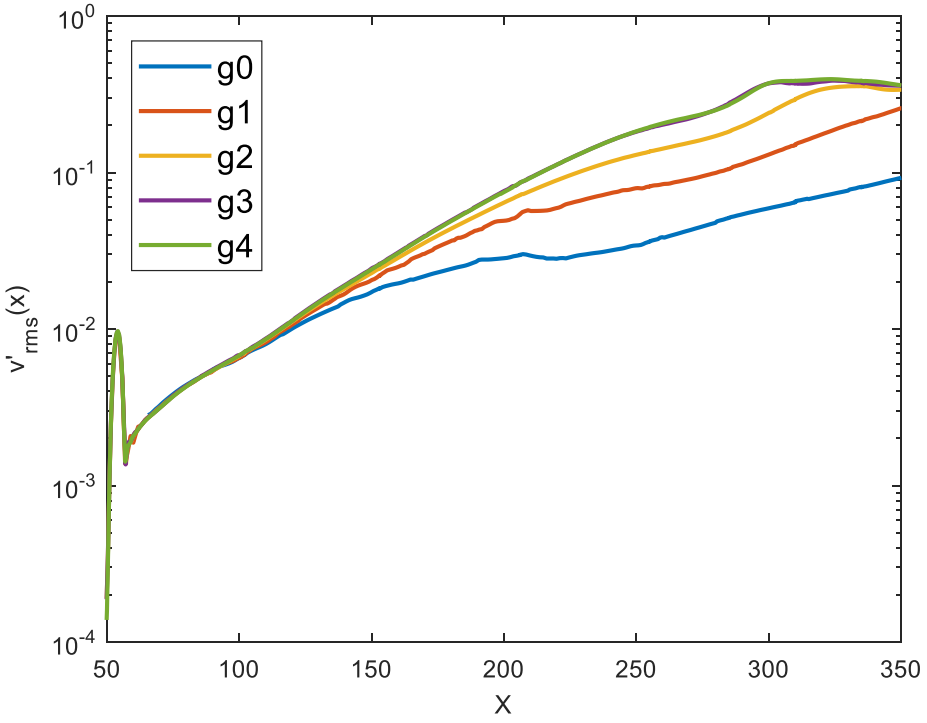

Figure 3 Root mean square of the wall-normal velocity distribution along the wall ($y = 0.7$) for different grid resolutions.

Linear Stability Analysis

A linear stability analysis was performed on the flat wall case to locate the position of the synchronization point, and to determine the proper location of the wall deformations. The synchronization point is the location where the phase velocities for the fast and slow modes are equal. The wall disturbance examined in the linearized stability analysis is the periodic blowing and suction. In Figure 4, the first and second modes are plotted based on the growth rates for various streamwise locations. The wavenumber of the first and second modes travels upstream as the streamwise travels downstream. When this occurs, the amplitude of the second mode increases, while the first mode amplitude does the opposite of the second mode amplitude.

The results from LST can be validated by comparing the first mode absolute values of the rho, u and P with the root-mean square values of rho, u and P. This comparison is displayed in Figure 5. The absolute values for the first mode components have been scaled accordingly to match the root-mean square values of the corresponding components. The curves for the rho, u and P components for the first mode match the curves for the root-mean square rho, u and P components very well; this comparison proves that the LSE method is quite accurate.

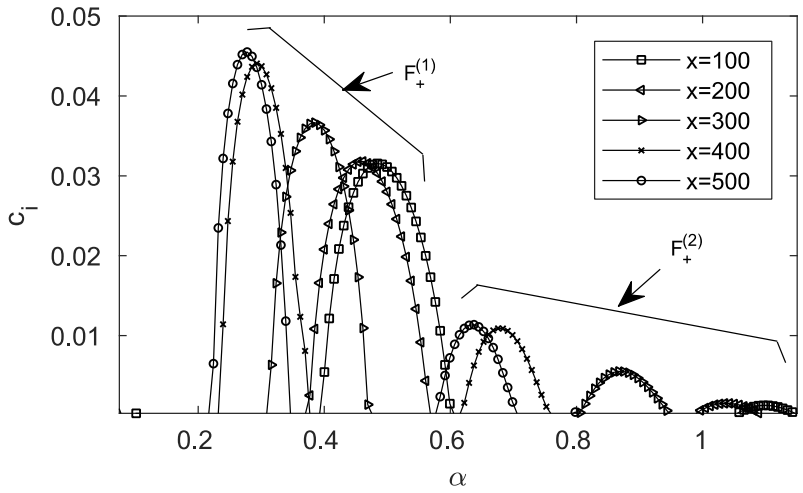

Figure 4 Growth rates for different streamwise locations.

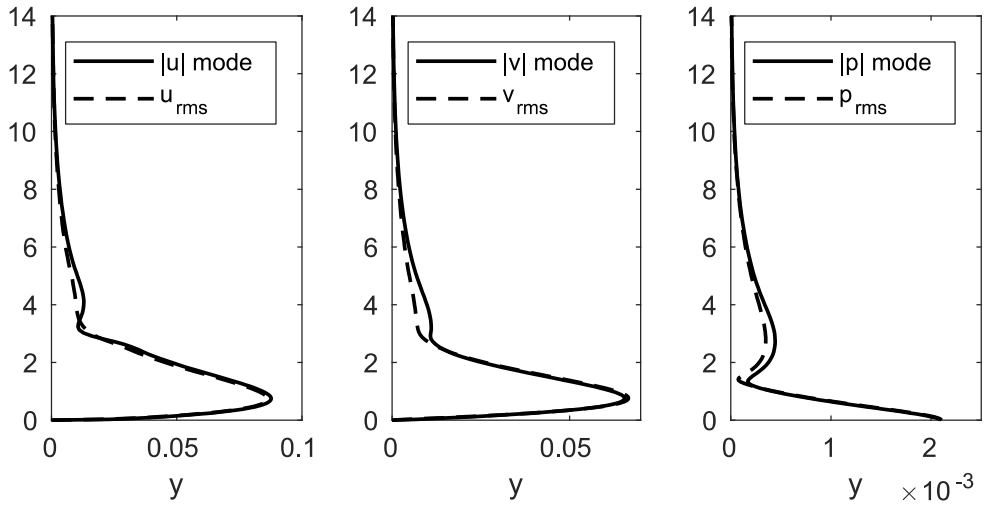

Figure 5 Comparison between the modes from linear stability analysis and the root mean square of u-velocity, v-velocity and pressure.

In order to identify the location of the synchronization point, the fast F and slow S modes are plotted to see where the two curves intersect. The location of the intersection corresponds to the wavenumber that can be used to calculate the location of the synchronization point. In Figure 6, the F and S modes are displayed, and based on the location of the intersection point, the synchronization point is found to be at x = 247.6.

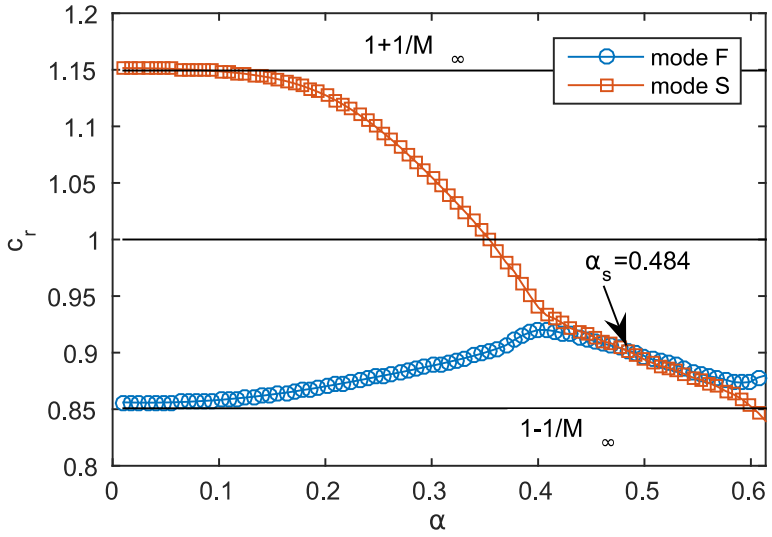

Figure 6 Phase velocities for the slow and fast waves as a function of the wavenumber.

Variation in Wall Deformation Shape

With the synchronization point located at x = 247.6 mm, the starting location for the wall deformation is required to be located downstream from this location. The location for the wall deformations to begin will be located at x = 300 mm in the flow domain, approximately half of the flow domain away from the leading edge. The wall deformations will have a height or a depth of 0.5 mm. Figure 7 displays the grids of the eight wall deformation cases that will be utilized to influence the boundary layer disturbances. The eight wall deformation cases are a backward step, forward step, surface dip, surface hump, sinusoidal wave of surface dips (sine 1), sinusoidal wave of surface humps (sine 2), a combination of a backward and forward step, and a combination of a forward and backward step. The grid mesh is compressed near the location of the wall deformation and then stretched to a uniform distribution outside of the wall deformation, so the $\Delta x = 0.1$ mm and $\Delta y = 0.01$ mm.

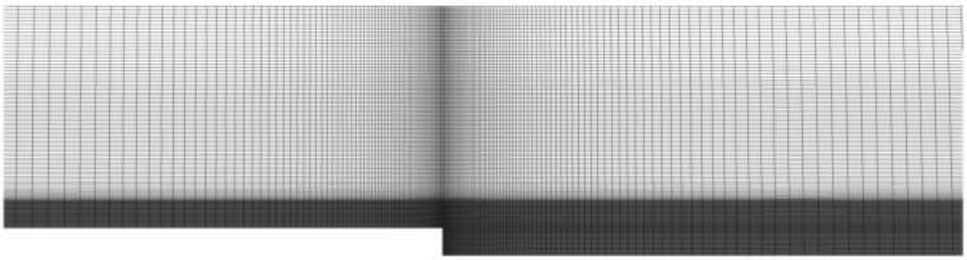

Figure 7 Computational grid meshes

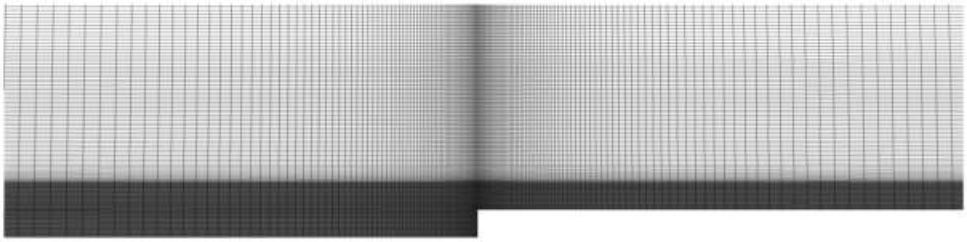

Figure 7b)

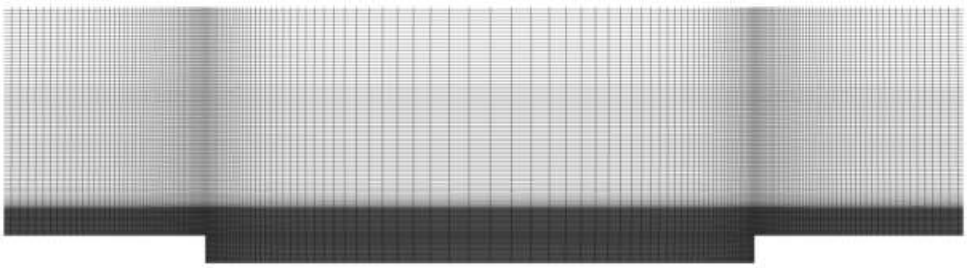

Figure 7c)

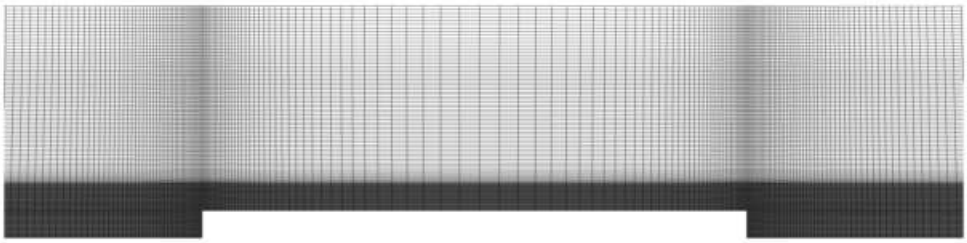

Figure 7d)

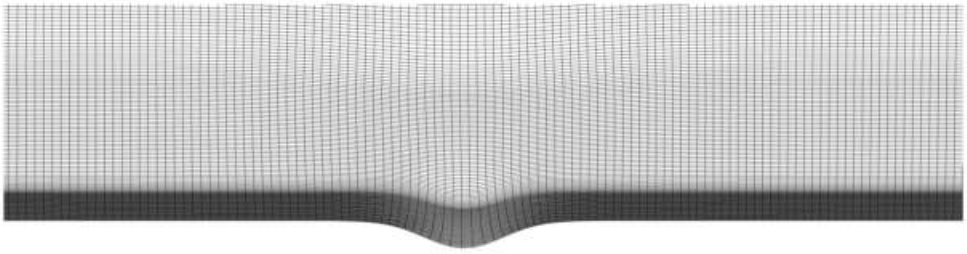

Figure 7e)

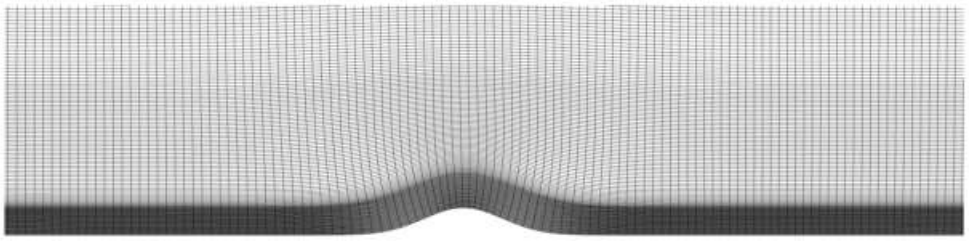

Figure 7f)

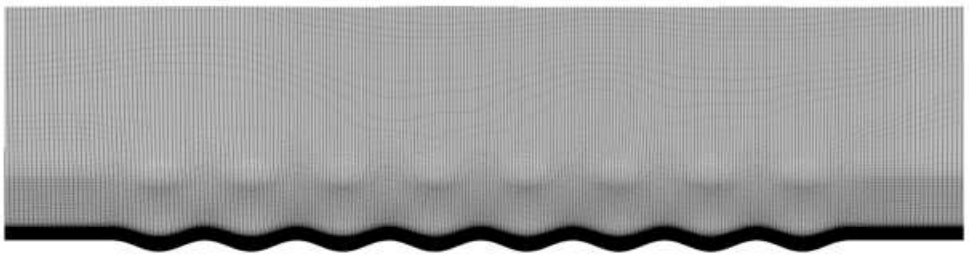

Figure 7g)

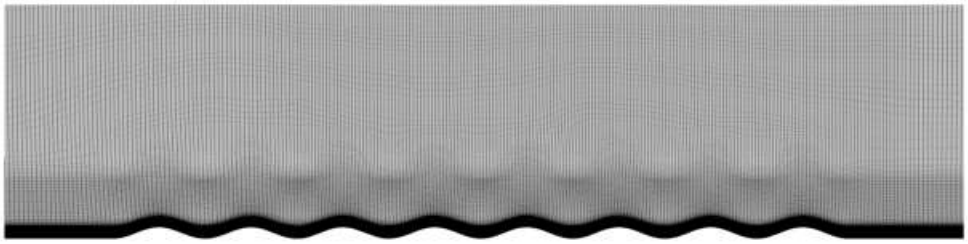

Figure 7h)

Mesh in the proximity to the surface deformation: a) backward step; b) forward step; c) combination of a backward and a forward step; d) combination of a forward and a backward step; e) surface dip; f) surface hump; g) wavy surface with the mean below the wall surface (successive dips); h) wavy surface with the mean above the wall surface (successive humps).

Before the two disturbances were applied to the wall deformation simulations, the mean flow of each deformation case was calculated using inflow profiles that were created for the compressible boundary layer defined as the beginning of the Results section. The mean pressure contour plots of the eight wall deformations were plotted in Figure 8. Every deformation created weak discontinuities that propagated to the external freestream flow field. The cases that produced the highest value discontinuities were the cases that began with a forward step or a surface hump, which were the forward step, surface hump, sine 2 and the combination case of a forward and backward step. The backward step, surface dip, sine 1 and the combination case of a backward step and forward step produced the weakest discontinuities.

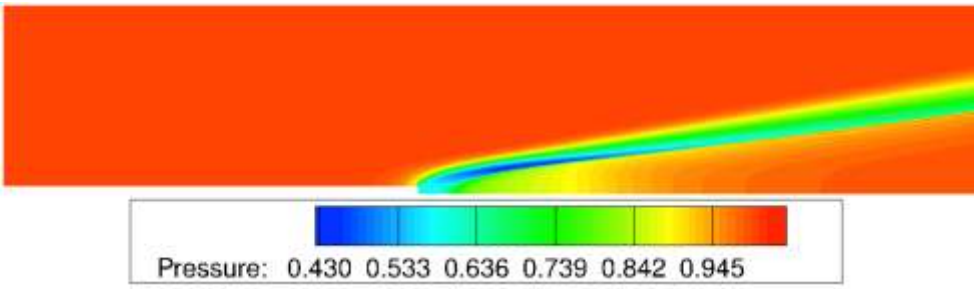

Figure 8 Mean pressure contours

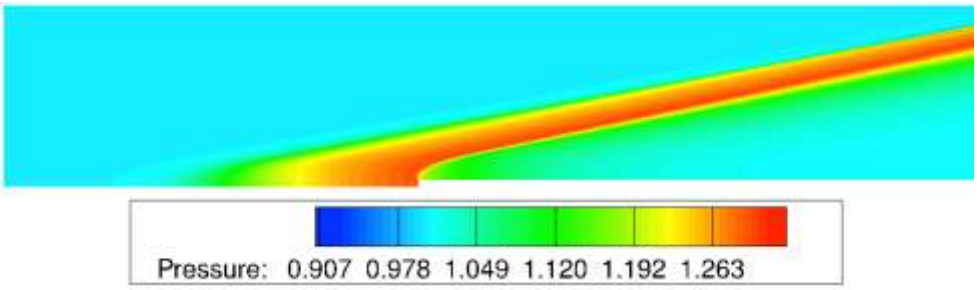

Figure 8b)

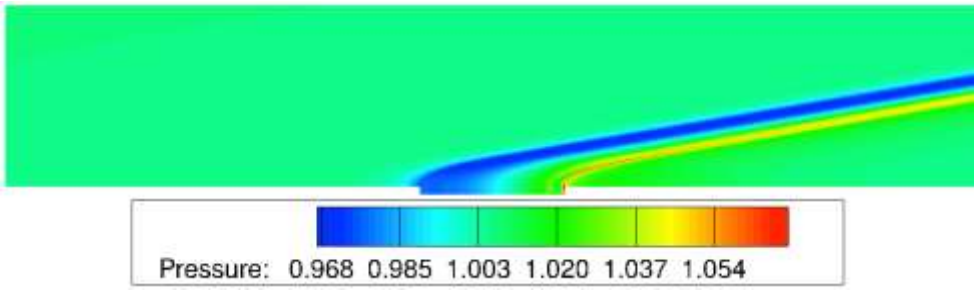

Figure 8c)

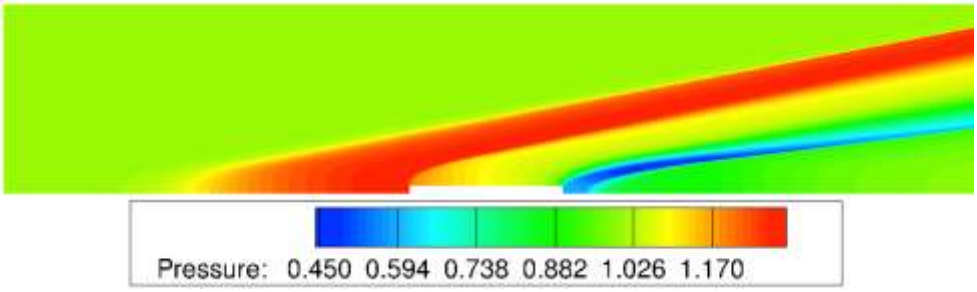

Figure 8d)

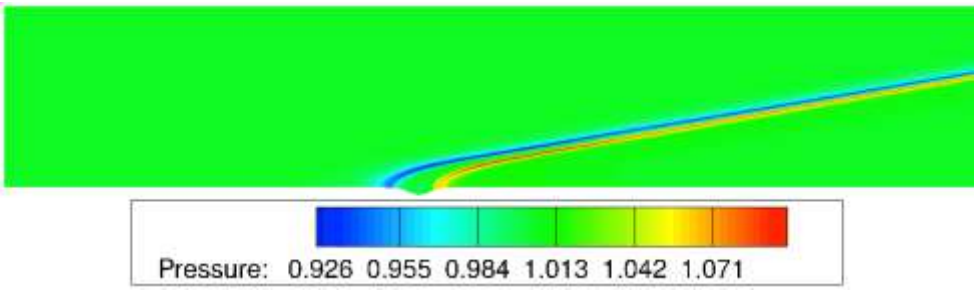

Figure 8e)

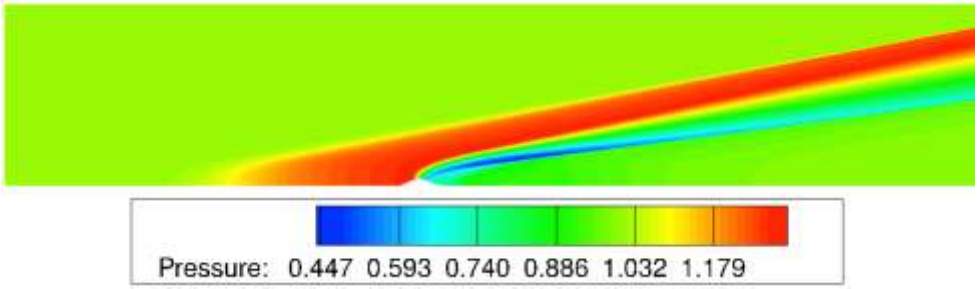

Figure 8f)

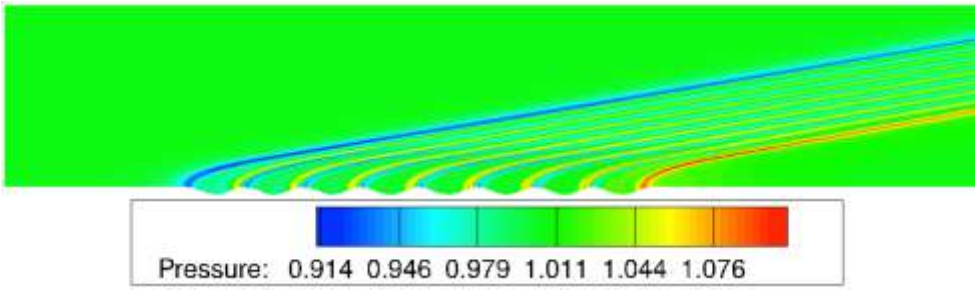

Figure 8g)

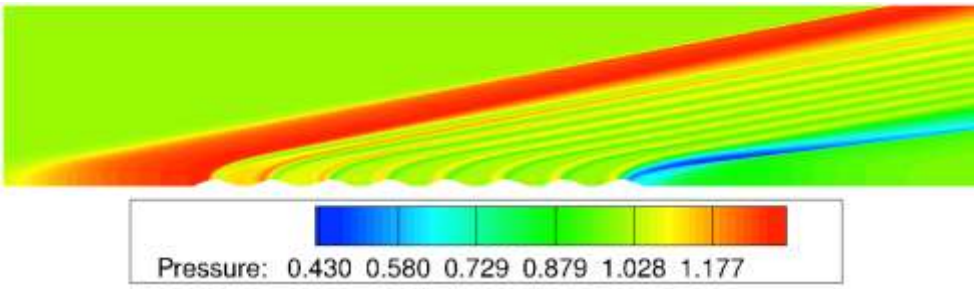

Figure 8h)

Mean pressure contours in the proximity to the surface deformation: a) backward step; b) forward step; c) combination of a backward and a forward step; d) combination of a forward and a backward step; e) surface dip; f) surface hump; g) wavy surface with the mean below the wall surface (successive dips); h) wavy surface with the mean above the wall surface (successive humps).

The mean pressure in the streamwise direction of the wall deformation cases are plotted in Figure 9 to quantitatively compare the cases to determine the extent of the discontinuity strengths. In the left plot of Figure 9, the backward step, forward step and the two combination cases were quantitative compared and the combination of the backward and forward step has the weakest distortion of the mean flow, while the forward step case and the combination of the forward and backward step had the greatest upstream distortion that were equal to one another. In the right plot, the surface dip, surface hump, sine 1 and sine 2 cases were plotted together to quantitatively compare to see which of the smooth curve deformation cases has the greatest distortion influence on the mean flow. Based on the plot, the dip and sine 1 cases had the weakest distortion to the mean flow, while the hump and sine 2 cases had the strongest distortion on the mean flow, with equal max distortion upstream of the wall deformation. The preliminary results from the mean flow distortions give a notable precursor to the potential results of how the wall deformations will affect the two wall disturbances, pulse and periodic oscillations. The wall deformations that exhibit a surface extruding from the surface of

the solid surface wall, such as the forward step, surface hump, sine 2 and combination case of forward and backward step, cause an increase in pressure with an associated adverse pressure gradient followed by a decrease in pressure with an associated favorable pressure gradient, or a succession of adverse and favorable pressure gradients (Sawaya et al). Based on this and the data in Figure 8, these cases will most likely dampen the disturbances that will be propagating within the boundary layer. The wall deformations with a drop in the solid surface wall, such as the backward step, surface dip, sine 1 and the combination case of a backward and forward step, have a favorable pressure gradient followed by an adverse pressure gradient, or a succession of adverse and favorable pressure gradients (Sawaya et al.[43]).

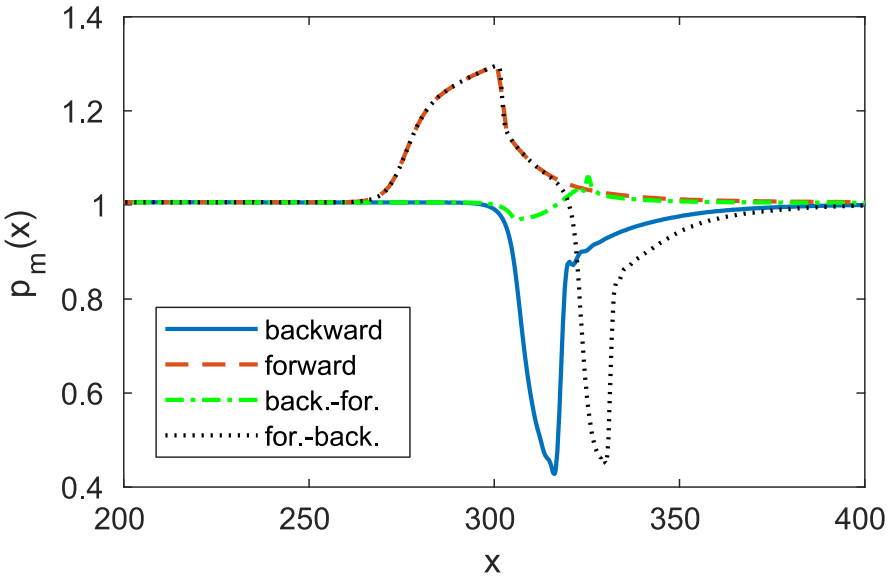

Figure 9 Mean pressure distribution

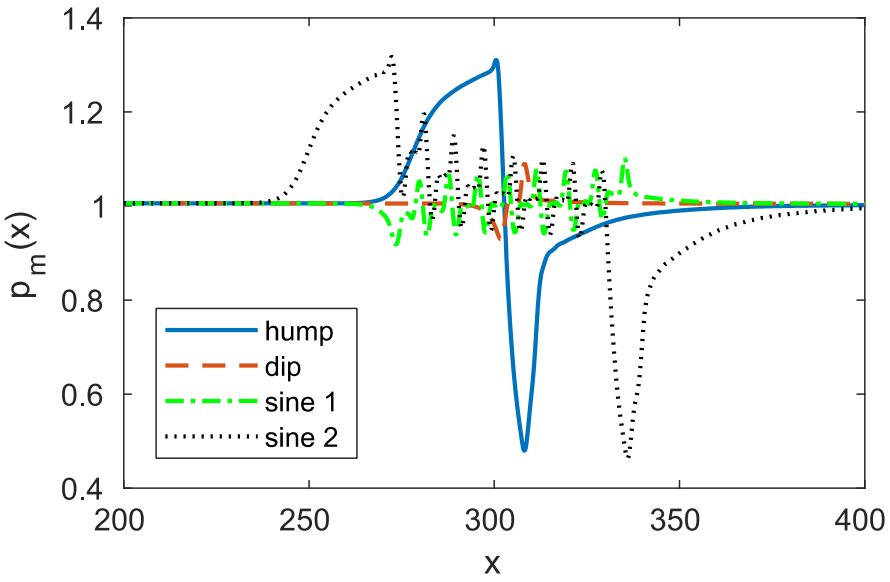

Figure 9 (continued)

Mean pressure distribution along the wall (y = 3), in the proximity to the surface deformation.

The periodic blowing and suction wall disturbance was applied to the eight wall deformation cases and the flat wall case. The disturbance pressure contour plots of the flat wall case and the eight wall deformations displayed in Figure 7, are shown in Figure 10 to notice the general influence of the wall deformation cases on the periodic oscillations occurring within the boundary layer. The flat wall case was also plotted as the baseline case for the eight wall deformation cases. From the figure, the discontinuity line that is caused by the forward step seems to divert the disturbances into the external flow and out of the boundary layer. This deviation of energy may be the explanation on the reduction of energy in the boundary layer due to the periodic disturbance. The contour plot for the combination case, Figure 10d, the diversion of the disturbance energy into the external flow is very minuscule compared to the forward step, due to the weak distortion and adverse pressure gradient displayed in Figures 8 and 9. The other cases

follow suite with the forward step or the combination case of the backward and forward steps, depending on the if the cases create a favorable or adverse pressure gradient.

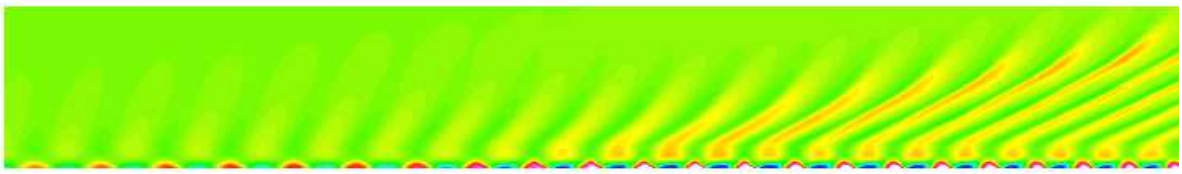

Figure 10 Pressure disturbance contours

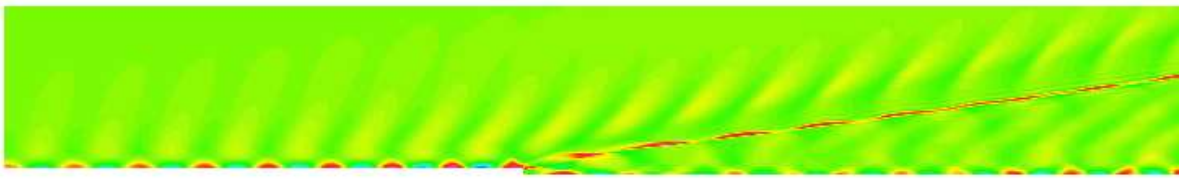

Figure 10b)

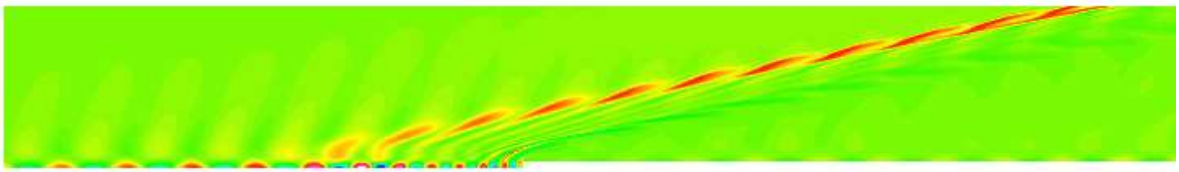

Figure 10c)

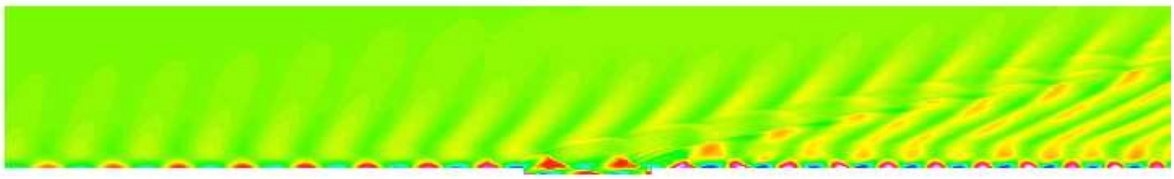

Figure 10d)

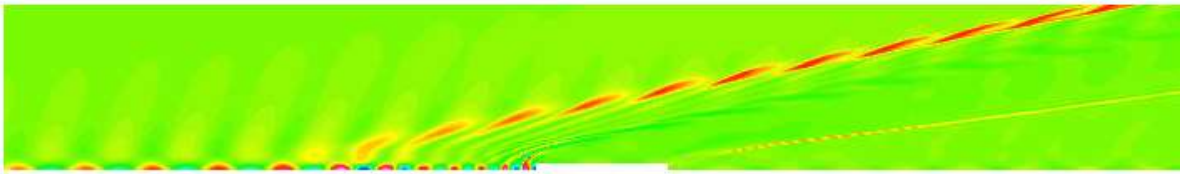

Figure 10e)

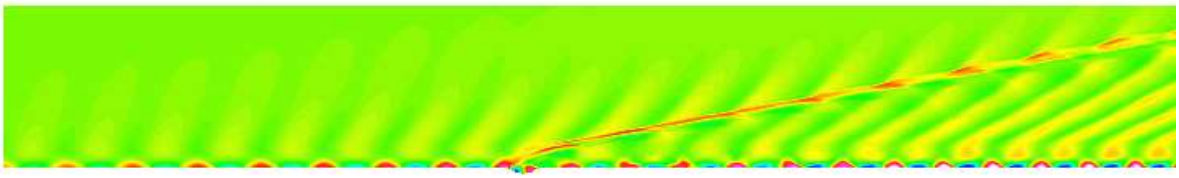

Figure 10f)

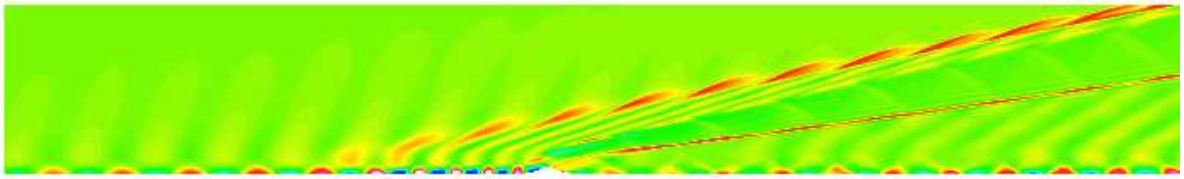

Figure 10g)

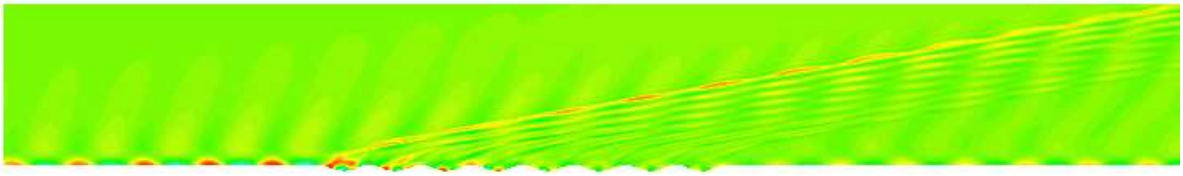

Figure 10h)

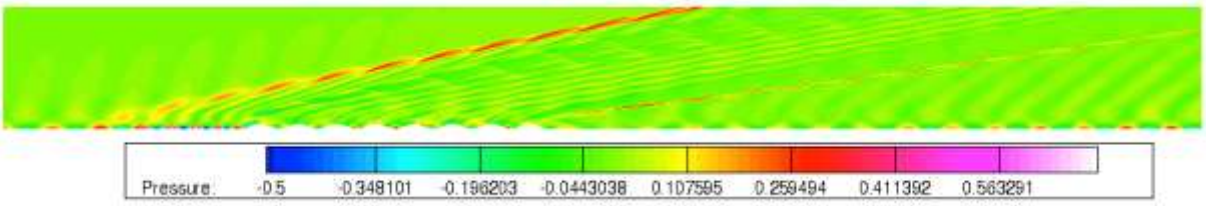

Figure 10i)

Pressure disturbance contours in the proximity to: a) flat wall; b) backward step; c) forward step; d) combination of a backward and a forward step; e) combination of a forward and a backward step; f) surface

dip; g) surface hump; h) wavy surface with the mean below the wall surface (successive dips); i) wavy surface with the mean above the wall surface (successive humps).

To support the assumption that the energy is deviated into the external flow, Figure 11 contains the contours of the time-averaged kinetic energy in the proximity to the wall deformations is plotted for the most effective roughness elements: forward step, surface hump and the wavy surface consisting of successive humps. The figure suggests that a portion of the kinetic energy is directed to the external flow, which does not occur in subsonic boundary layers since there are no discontinuities posed by the roughness element. However, the deviated portion of the energy is small with respect to the upstream kinetic energy level, approximately 10%, so this may not be the main mechanism of the disturbance energy reduction, but a factor to be taken into account.

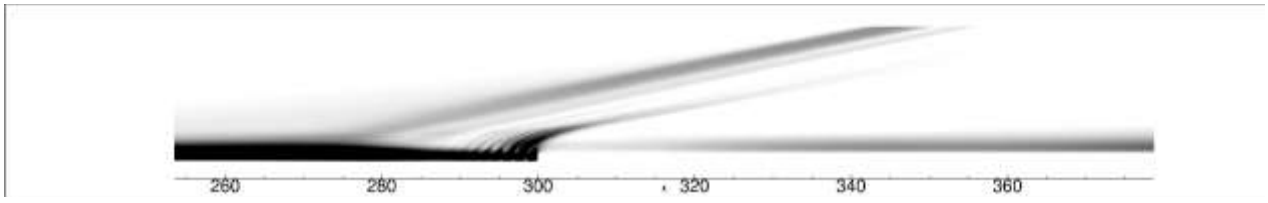

Figure 11 Time-averaged kinetic energy contours

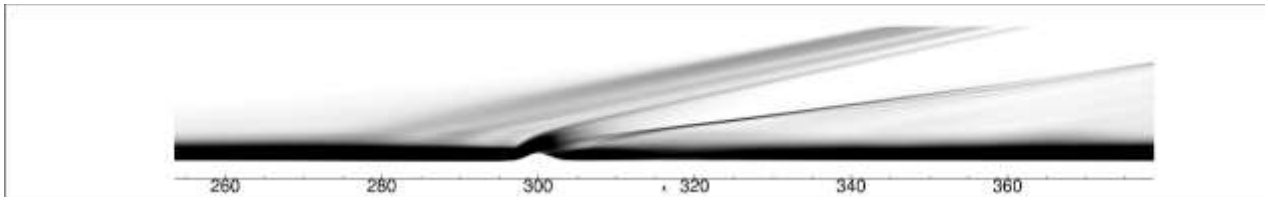

Figure 11b)

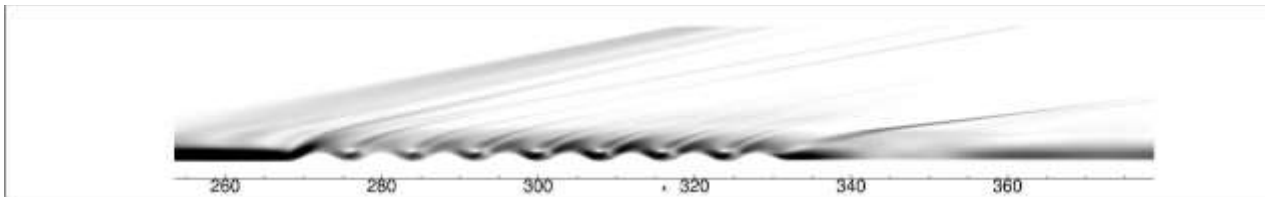

Figure 11c)

Time-averaged kinetic energy contours in the proximity to the surface deformations: a) forward step; b) surface hump; c) wavy surface consisting of successive humps. The ratio between 'grey' and 'black' patches is approximately 1/10.

The disturbance energy reduction from each of the cases are quantitatively plotted in Figures 12 and 13, where the energy reduction in the stream wise direction is plotted. The root-mean square velocity normal to the wall is plotted for the pulse disturbance and the periodic blowing and suction disturbance, respectively, and the wall deformation cases are compared to the flat wall results. For the pulse disturbance, the sine 2 and combination case of a forward and backward step had the greatest reduction in the disturbance amplitude, while the dip case had to smallest reduction in disturbance amplitude. For the periodic blowing and suction disturbance, the sine 1, sine 2, forward step and combination case of the forward step and backward step had the greatest reduction in the disturbance amplitude, while the dip and combination case of the backward step and forward step seemed to have the lowest reduction overall of the periodic disturbance amplitude. The hump case and the backward step case had moderate reduction in disturbance amplitude for the both sets of boundary layer disturbances. This moderate reduction of the amplitude is from the change in the wall surface.

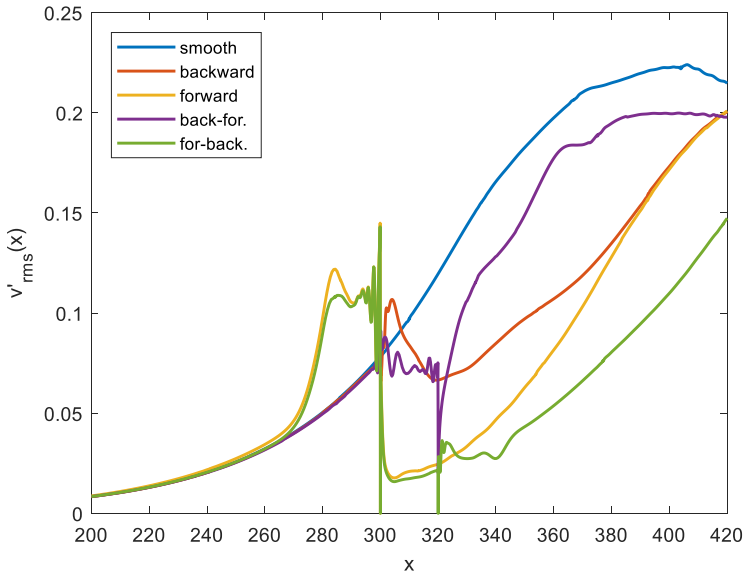

Figure 12 V-rms pulse disturbance in x-direction

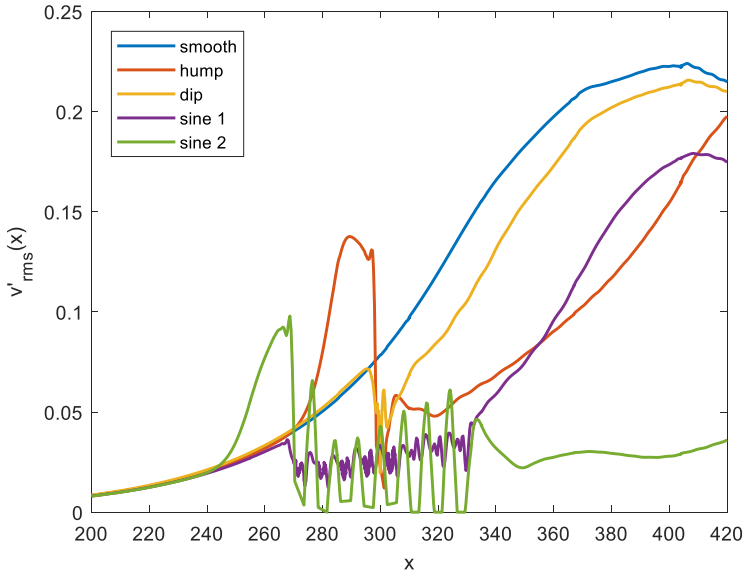

Figure 12b)

Root mean square of the wall-normal velocity distribution along the wall (y = 0.7) for the pulse disturbance.

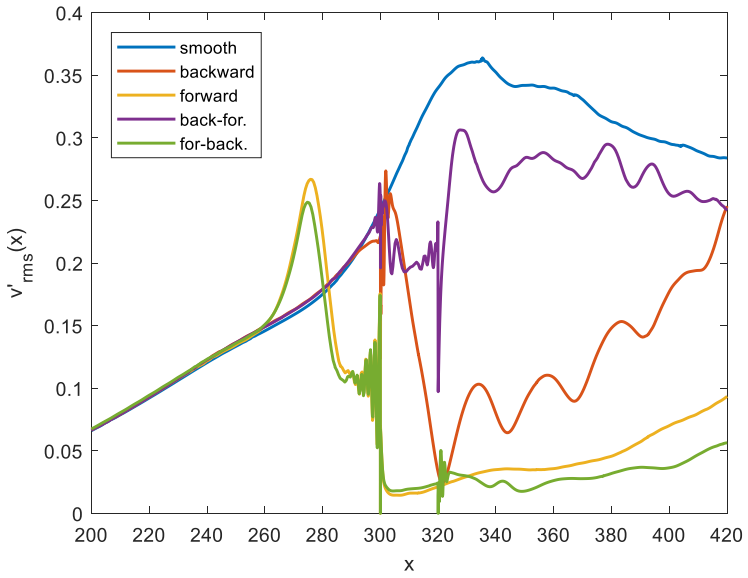

Figure 13 V-rms blowing and surction disturbance in x-direction

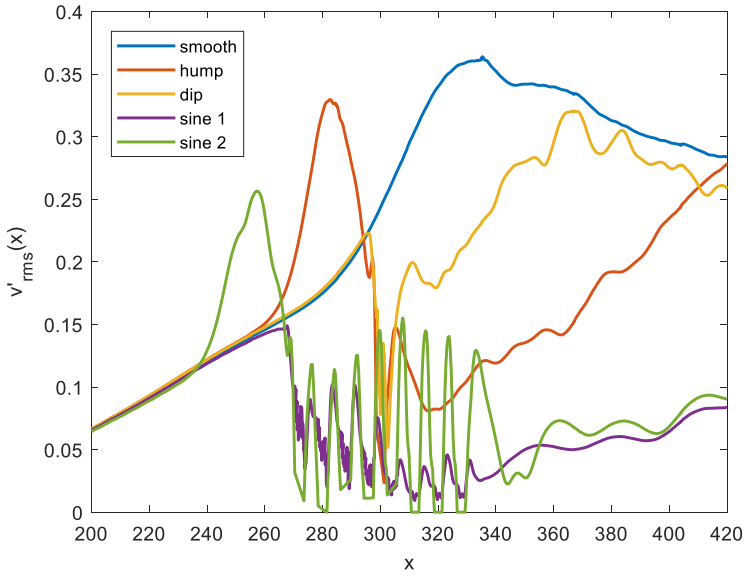

Figure 13 (continued)

Root mean square of the wall-normal velocity distribution along the wall (y = 0.7) for the periodic flowing and suction disturbance.

The wall-normal velocity of the simulation cases in the vertical direction are plotted in Figure 14 and 15 for the pulse and periodic blowing and suction wall disturbances respectively. The analysis for these plots was chosen at x = 350 mm, which is downstream from the wall deformation. Based on the plots, most of the disturbance kinetic energy resides within the boundary layer, which is approximately 3.5 mm thick. The forward step, sine 2 case and the combination of the forward step and the backward step case had the overall smoothest wall-normal velocity profiles for the two disturbances. For the pulse disturbance, the sine 2 case had the smoothest velocity profile. The combination of the forward step and backward step case had the smoothest velocity profile for the periodic blowing and suction disturbance. All the cases that create an extrusion of the wall surface, as compared to the flat wall case, and the sine 1 and backward step cases have a noticeable influence on the reduction in the wall disturbance amplitude. While the dip and combination of the backward step and forward step cases seem to have minor influence on the reduction on the wall disturbance amplitude.

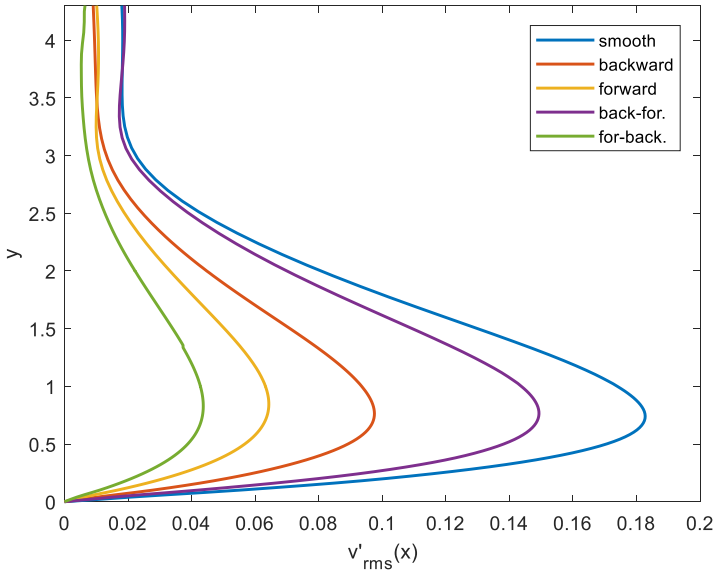

Figure 14 V-rms pulse disturbance in y-direction

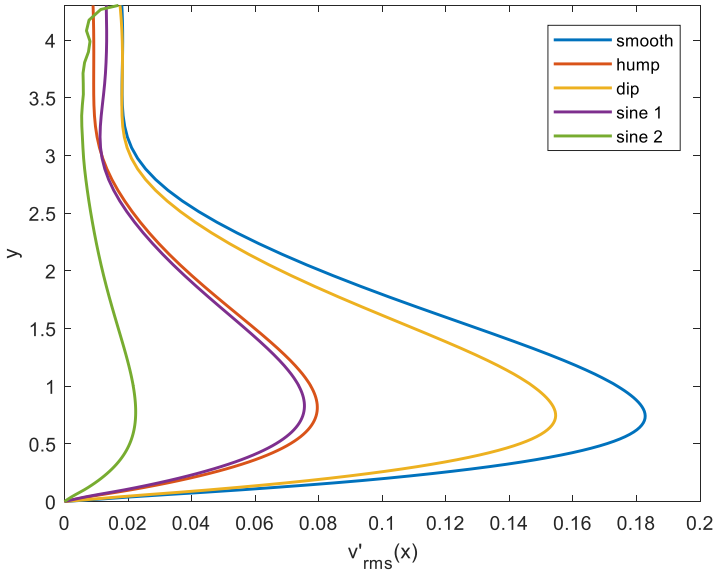

Figure 14 (continued)

Profiles of root mean square of wall-normal velocity (x = 350) for the pulse disturbance.

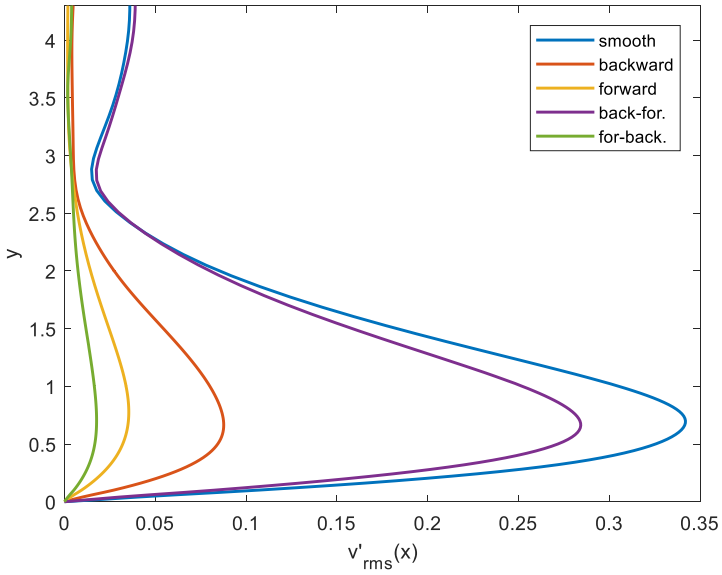

Figure 15 V-rms blowing and suction disturbance in y-direction

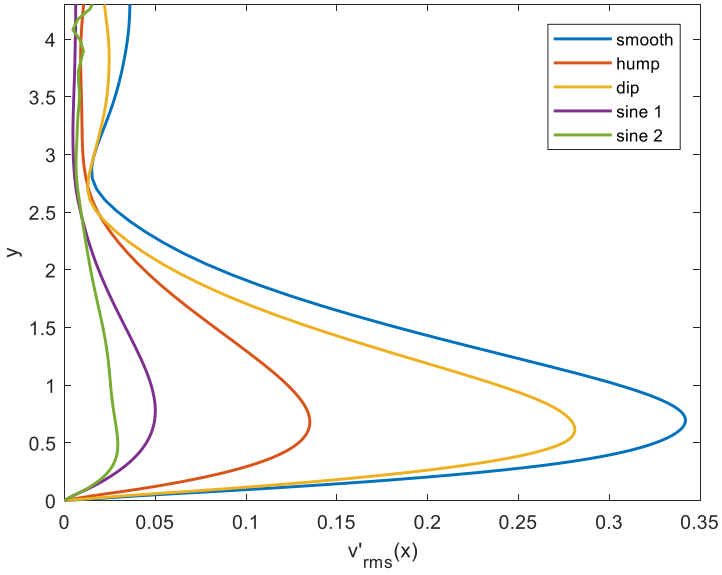

Figure 15 (continued)

Profiles of root mean square of the wall-normal velocity (x = 350) for the periodic blowing and suction disturbance.

In Figures 16, the root mean square of the pressure is plotted for the periodic blowing and suction disturbance, respectively. The trends in the figures agree with the trends seen in Figure 15 for the wall deformation cases, where the forward step, combination of forward and backward step and sine 2 have the greatest reduction in disturbance energy of the periodic blowing and suction disturbance within the boundary layer. While the combination of a backward and forward step, and dip cases have the least amount of reduction in the disturbance energy within the boundary layer.

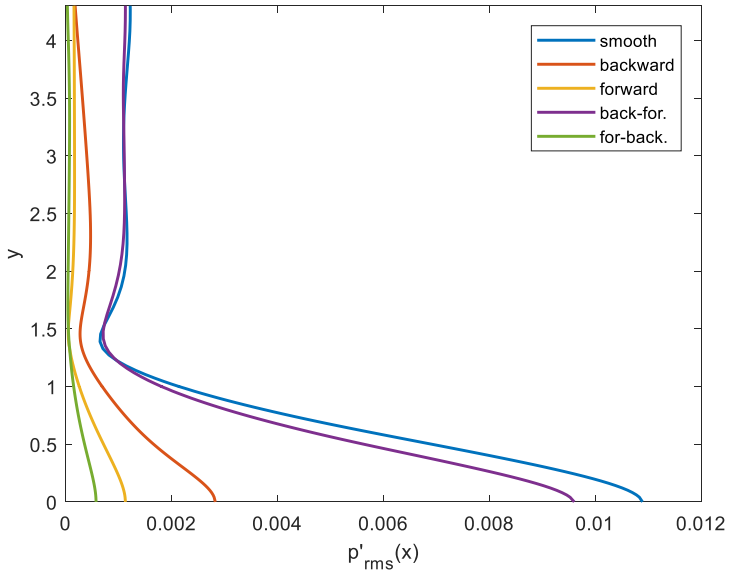

Figure 16 P-rms of blowing and suction disturbance in y-direction

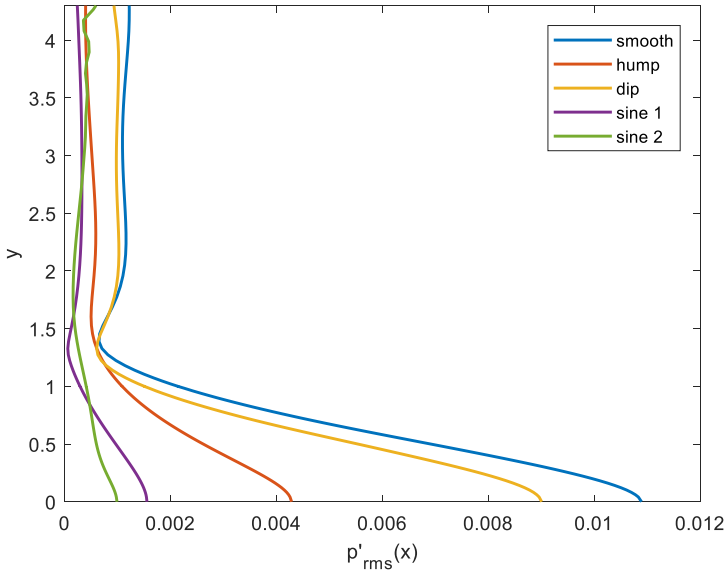

Figure 16b)

Profiles of root mean square of the pressure (x = 350) for the periodic blowing and suction disturbance.

Variation in Wall Deformation's Streamwise Extent

In this section, the dependency of the energy reduction on the streamwise width of the deformation is investigated for the backward-forward step combination, forward-backward combination, surface hump, surface dip, sine 1 consisting of successive dips and sine 2 consisting of successive humps. Figure 17 shows the two backward-forward step configurations that are considered: one has the streamwise length of 20 and the other length of 40 step heights. In figure 18a, the mean pressure distribution along the wall reveals that the extension of the width between the backward and the forward steps poses a greater distortion in the mean flow, compared to its smaller width. This is because the boundary layer flow in the second case (greater width) has enough room for the flow to adjust itself to the original upstream condition, so the interaction with the

forward step becomes stronger; in other words, the two flows near the wall deformations are less affected by each other as the width is increased. However, in figure 18b, one can notice that the two deformations have almost the same effect on the propagating disturbance.

Figure 17 Backward-forward streamwise meshes

Figure 17 (continued)

Combination of a backward and forward step shapes with different streamwise width.

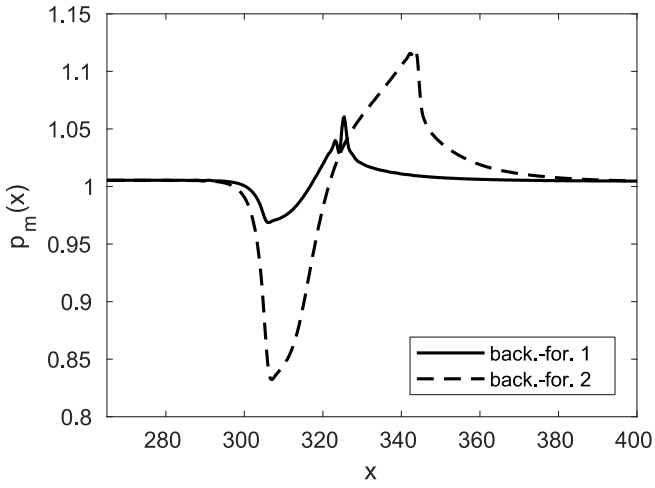

Figure 18 backward-forward streamwise width distribution plots

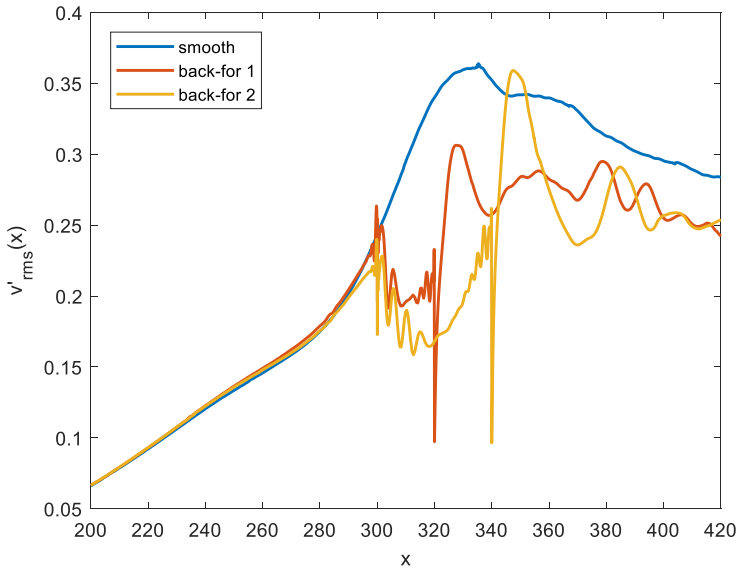

Figure 18b)

a) Mean pressure distribution along the wall (y = 1); b) Root mean square of the wall-normal velocity distribution along the wall (y = 0.7).

The same analysis is performed for the forward-backward combination, as shown in figure 19, where the first figure corresponds to a streamwise width of 12 step heights, while the second figure corresponds to a width of 20 step heights. The upstream adverse pressure gradient in figure 20a does not reveal a difference between the two cases, while there is some difference in the favorable pressure gradient portion in the downstream. Anyway, the effect on the disturbance propagation is almost the same, as displayed by distributions of root mean square of the wall-normal velocity distribution in figure 20b.

Figure 19 Forward-backward streamwise meshes

Figure 19 (continued)

Combination of a forward and backward step shapes with different streamwise width.

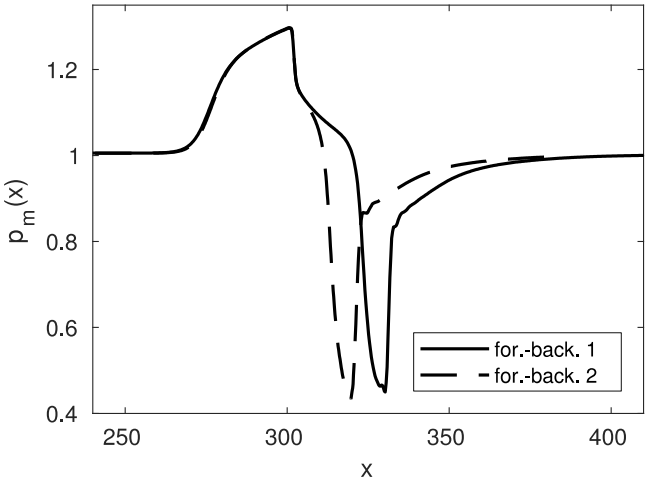

Figure 20 Forward-backward streamwise distribution plots

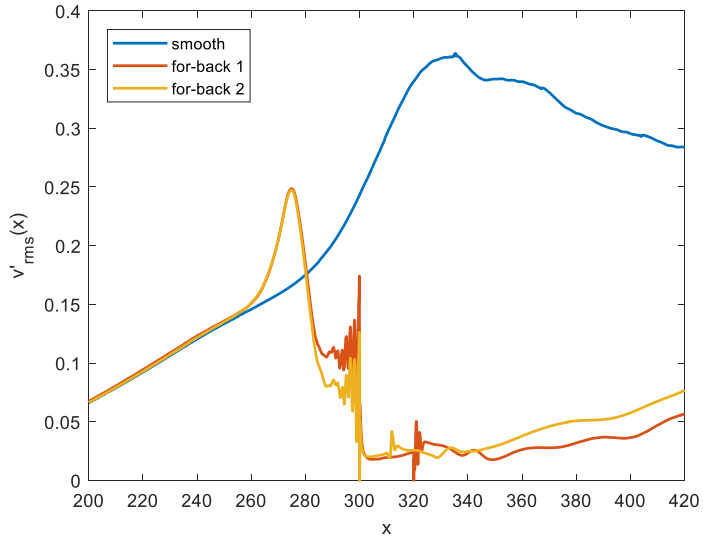

Figure 20b)

a) Mean pressure distribution along the wall (y = 1); b) Root mean square of the wall-normal velocity distribution along the wall (y = 0.7).

Increasing the streamwise width of the surface hump, shown in figure 21, has an effect in the mean pressure distribution as shown in figure 22a, but not very significant. When concerning the root mean square of the wall-normal velocity, shown in figure 22b, the increase in the streamwise width of the surface hump deformation results in a less significant reduction of the disturbance amplitudes. Thus, leading to the conclusion that a shorter, more localized surface hump should be utilized to reduce the disturbance energy. In Fong et al.[17], the opposing results were obtained pertaining to a surface hump deformation, but the surface roughness considered in that study was not smooth, where the wall and the roughness element meet; and the disturbance utilized in the Fong et al. study was a pulse propagating as a wave packet, while the disturbance in this study is periodic.

Figure 21 Surface hump streamwise meshes

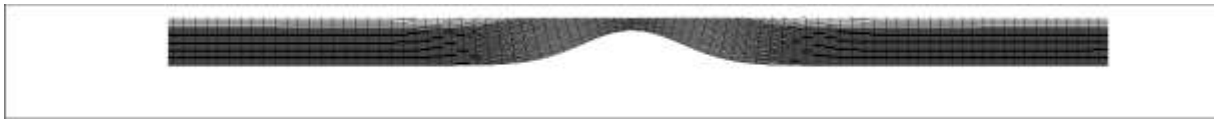

Figure 21 (continued)

Figure 21 (continued)

Surface hump shapes with different streamwise width.

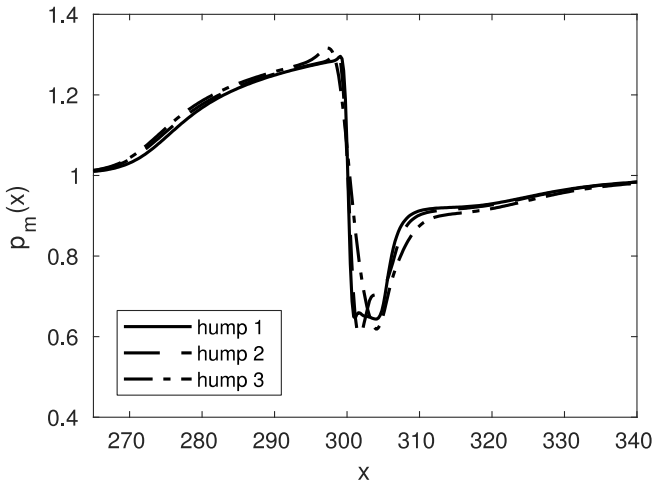

Figure 22 Surface hump streamwise distribution plots

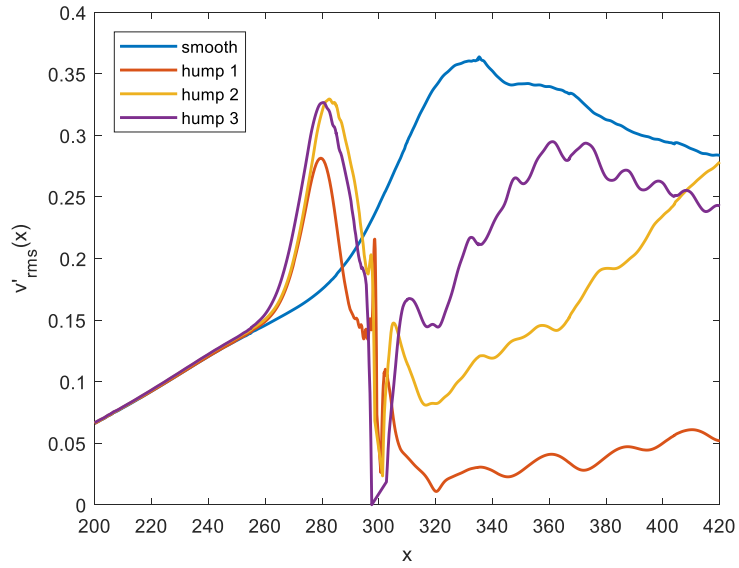

Figure 22b)

a) Mean pressure distribution along the wall (y = 1); b) Root mean square of the wall-normal velocity distribution along the wall (y = 0.7).

In contrast to the surface hump deformation, increasing the streamwise width of the surface dip, shown in figure 23, proportionately affects the mean flow shown in figure

24a. An interesting result is observed in figure 24b, where the root mean square of the wall-normal velocity is greatly reduced for the shortest and longest streamwise dip, while the root mean square for the intermediate surface dip has a smaller reduction.

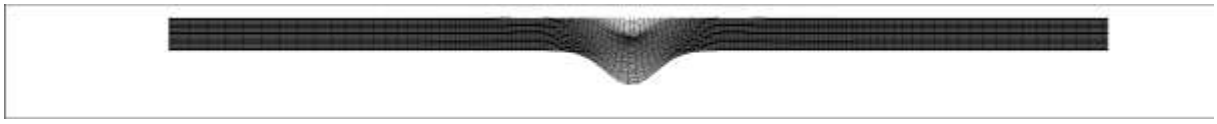

Figure 23 Surface dip streamwise meshes

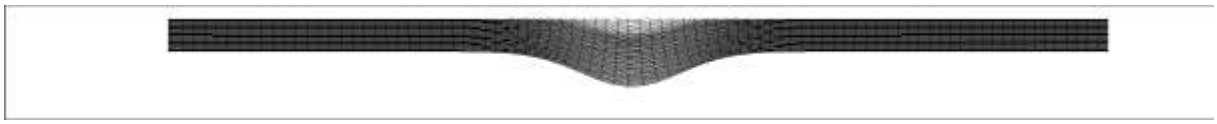

Figure 23 (continued)

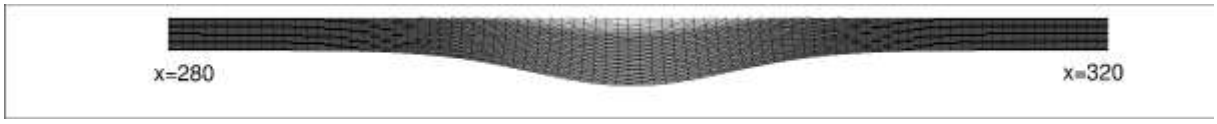

Figure 23 (continued)

Surface dip shapes with different streamwise width.

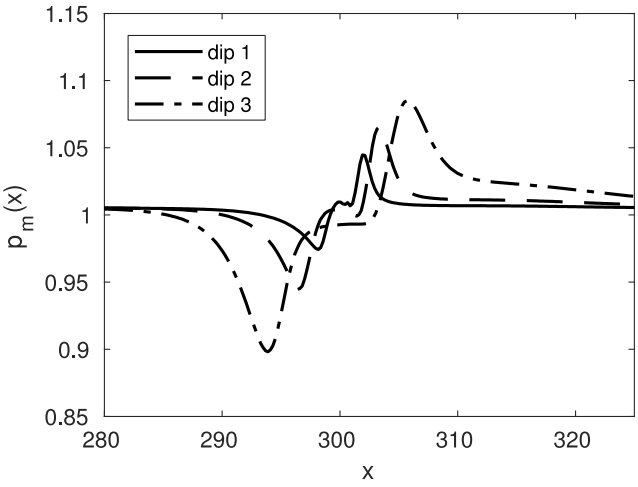

Figure 24 Surface dip streamwise distribution plots

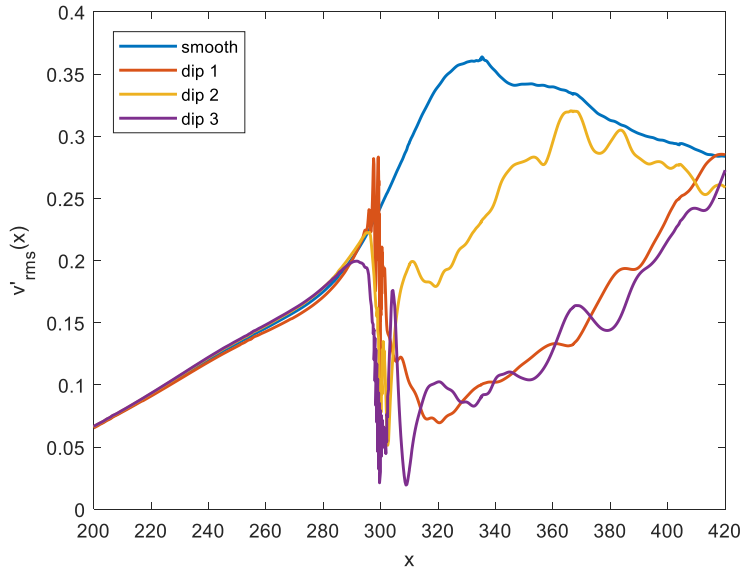

Figure 24b)

a) Mean pressure distribution along the wall (y = 1); b) Root mean square of the wall-normal velocity distribution along the wall (y = 0.7).

The next set of results refer to the wavy surface consisting of successive surface dips (sine 1) and the wavy surface consisting of successive humps, to determine the effect of the varying wavenumber associated with the sine function utilized to generate the deformations. The shape of the deformation in figure 25 correspond to sine 1

deformation, with the middle shape as the original sine 1 deformation used in the previous results section. The distributions of the mean pressure near the wall (y = 1) are plotted in figure 26a. The mean pressure is shown to increase as the wavenumber of the wavy surface deformation is decreased. This result is prominent when comparing the first sine 1 shape with the third sine 1 shape. There is no significant impact of the wavy surface wavenumber on the disturbance amplitude, as shown in figure 26b where the root mean square of the wall-normal velocity distribution for the three sine 1 shapes.

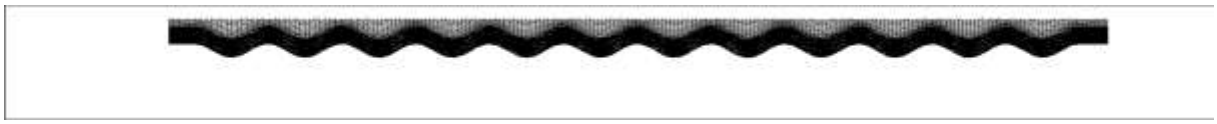

Figure 25 Wavy surface (sine 1) streamwise meshes

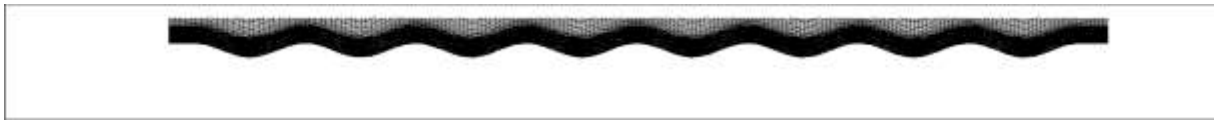

Figure 25 (continued)

Figure 25 (continued)

Wavy surface consisting of successive surface dip (sine 1) shapes with different streamwise width.

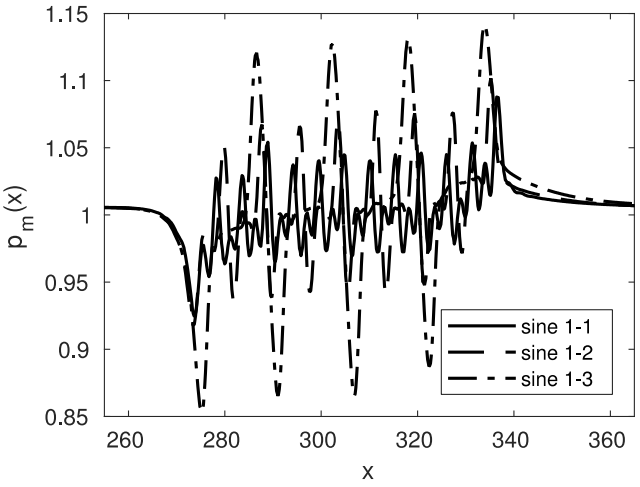

Figure 26 Wavy surface (sine1) streamwise distribution plots

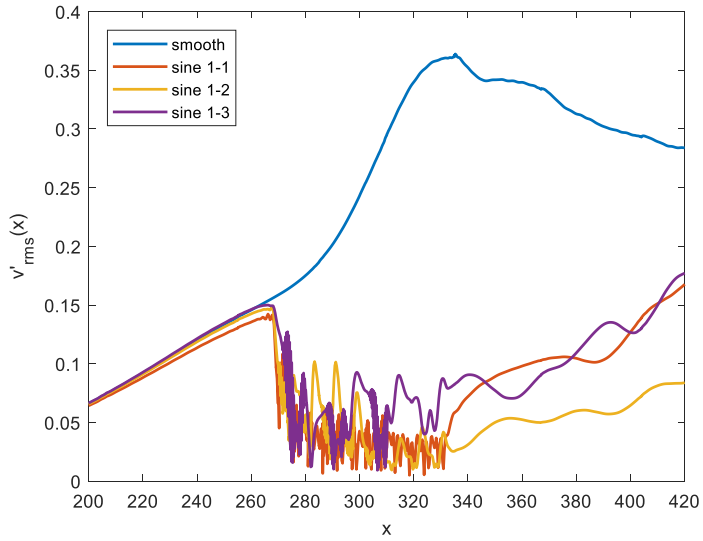

Figure 26b)

a) Mean pressure distribution along the wall (y = 1); b) Root mean square of the wall-normal velocity distribution along the wall (y = 0.7).

The shape of the deformation in figure 27 correspond to sine 2 deformation, with the middle shape being utilized in the previous results section. The distributions of the mean pressure near the wall (y = 1) are plotted in figure 28a. The mean pressure is shown to increase as the wavenumber of the wavy surface deformation is decreased, but not as

significantly as the sine 1 deformation. There is no significant impact of the wavy surface wavenumber on the disturbance amplitude, as shown in figure 28b where the root mean square of the wall-normal velocity distribution for the three sine 2 shapes.

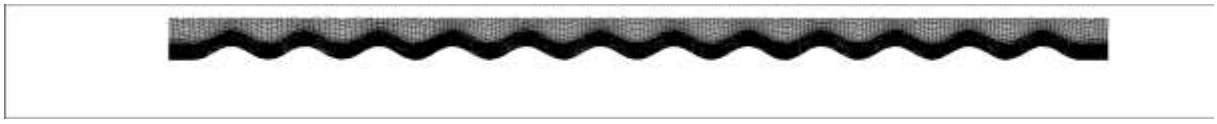

Figure 27 Wavy surface (sine 2) streamwise meshes

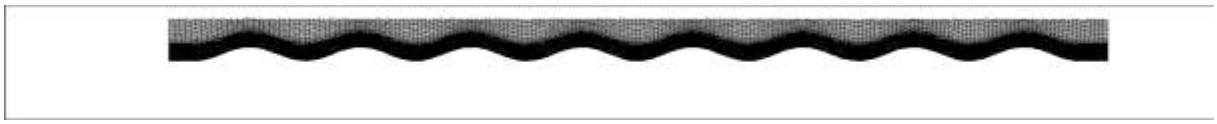

Figure 27 (continued)

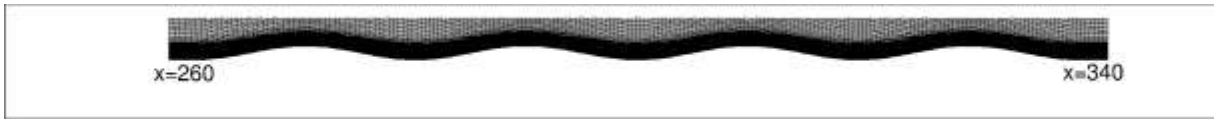

Figure 27 (continued)

Wavy surface consisting of successive surface hump (sine 2) shapes with different streamwise width.

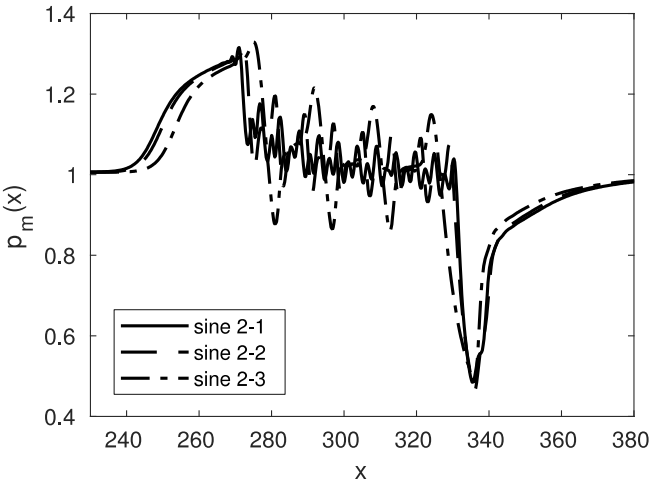

Figure 28 Wavy surface (sine 2) distribution plots

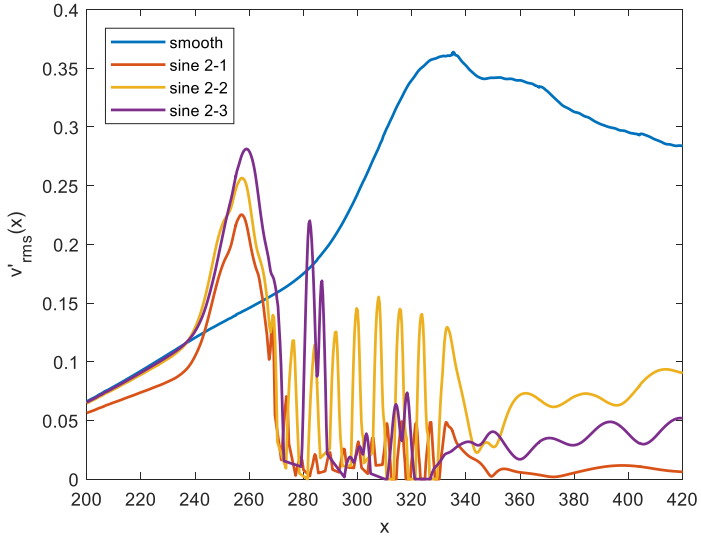

Figure 28b)

a) Mean pressure distribution along the wall (y = 1); b) Root mean square of the wall-normal velocity distribution along the wall (y = 0.7).

Variation of wall deformation height

In Fong et al.[15-17], the roughness element location and height was extensively studied. In this section, the deformation heights are varied for three different cases: 0.25mm, 0.5mm (original), 0.75mm. Figure 29 represents the deformation cases

involving a sudden change in the surface, such as the backward or forward step. The forward step, backward step and combination of the forward and backward step cases follow a similar trend that when the deformation height was increased from 0.5mm to 0.75mm, the periodic disturbance amplitude was reduced as compared to the original height. When the deformation height was reduced to 0.25mm, the periodic disturbance amplitude is not reduced as much as the original height of the deformation tested in the previous sections of the Results. These results are conclusive with the results presented in the Fong et al.[15-17]. The combination of the backward and forward step case, the data is not very conclusive. When the step height is reduced to 0.25mm and then increased to 0.75mm, both seem to reduce the periodic disturbance amplitude as compared to the original deformation height. Future work will allow for some clarification for this result displayed in Figure 29c.

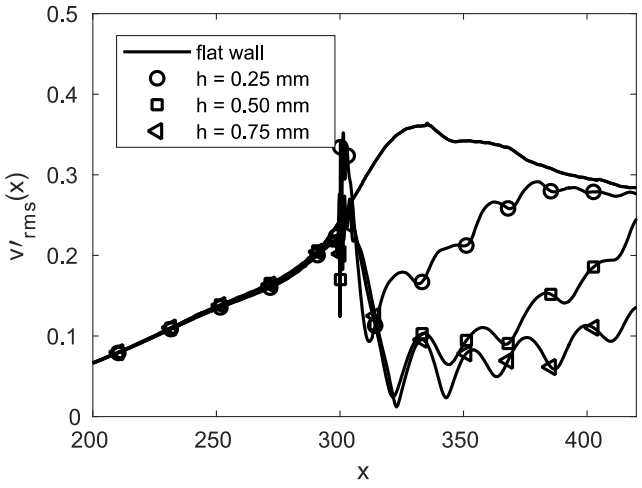

Figure 29 Variation in discontinuous deformation heights

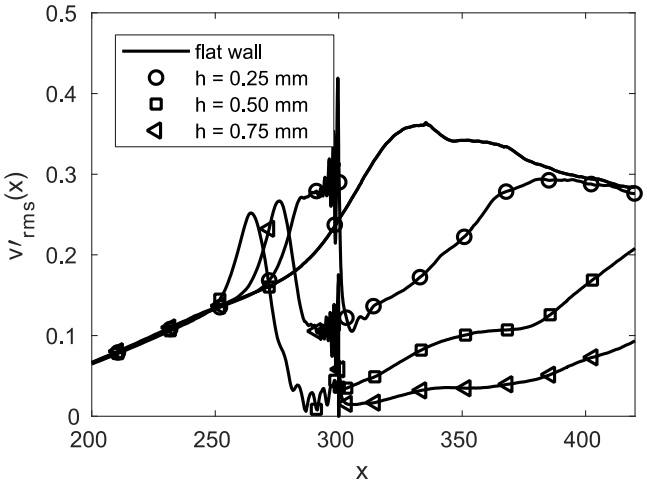

Figure 29b)

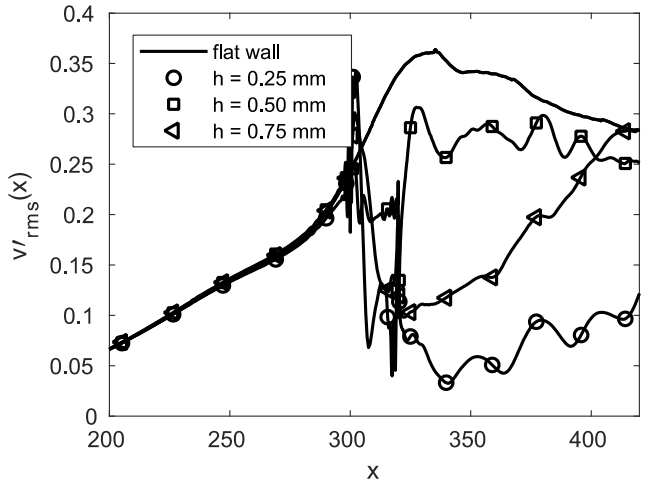

Figure 29c)

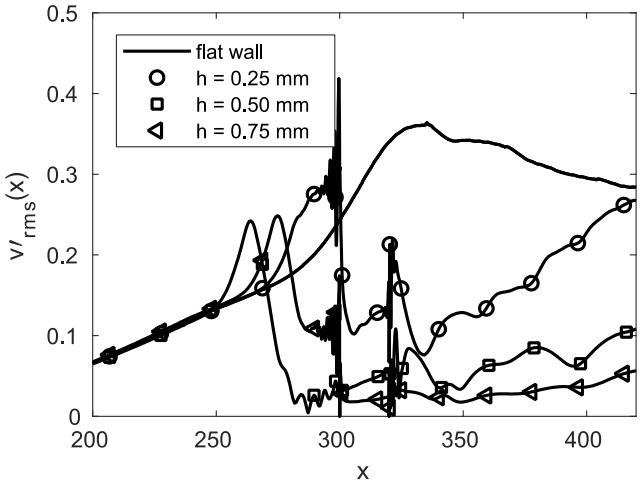

Figure 29d)

Root mean square of the wall-normal velocity distribution along the wall (y = 0.7): a) backward step; b) forward step; c) combination of backward and forward steps; d) combination of forward and backward steps.

Figure 30 represents the deformation cases involving a continuous change in the surface, such as the surface dip or surface hump cases. The surface hump and sine 2 cases are conclusive with the forward step case above and the results presented in the Fong et al.[15-17]. The surface dip and sine 1 cases, the data is not very conclusive. When the step height is reduced to 0.25mm and then increased to 0.75mm, both seem to reduce the periodic disturbance amplitude as compared to the original deformation height. Future work will allow for some clarification for this result displayed in Figure 30b and Figure 30c.

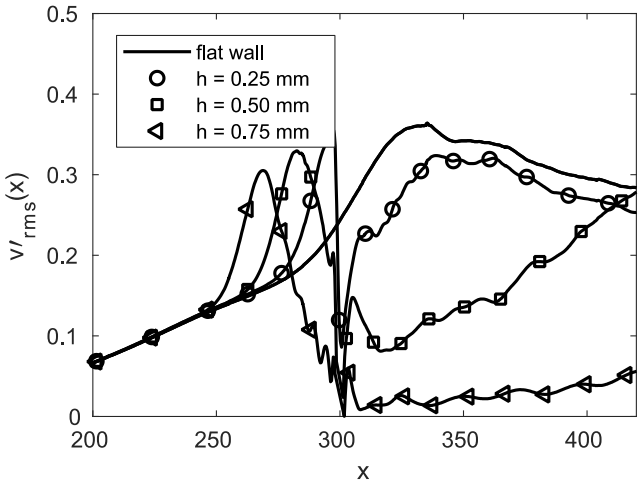

Figure 30 Variation in continuous deformation heights

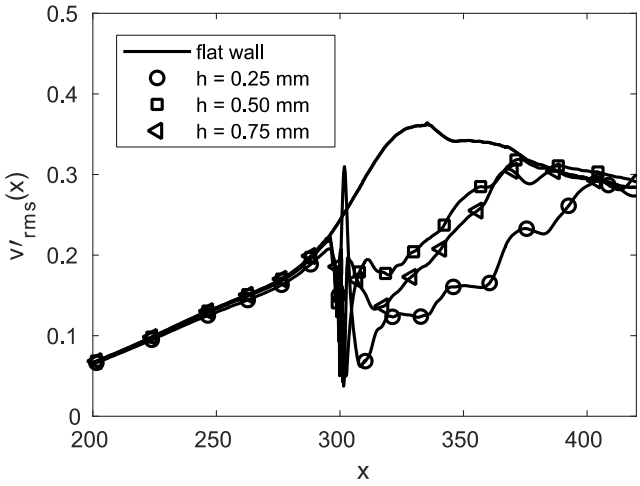

Figure 30b)

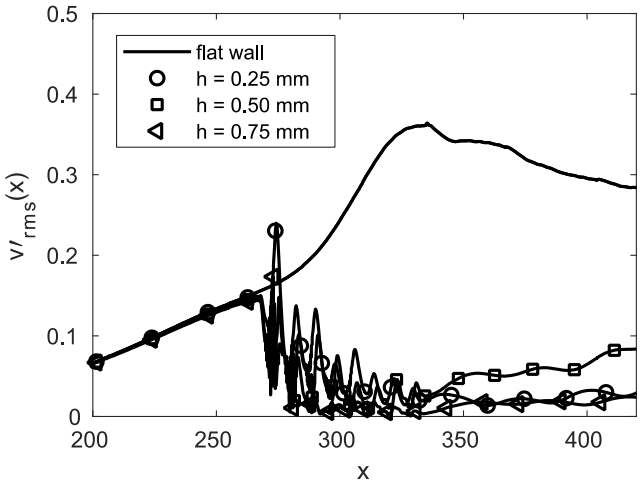

Figure 30c)

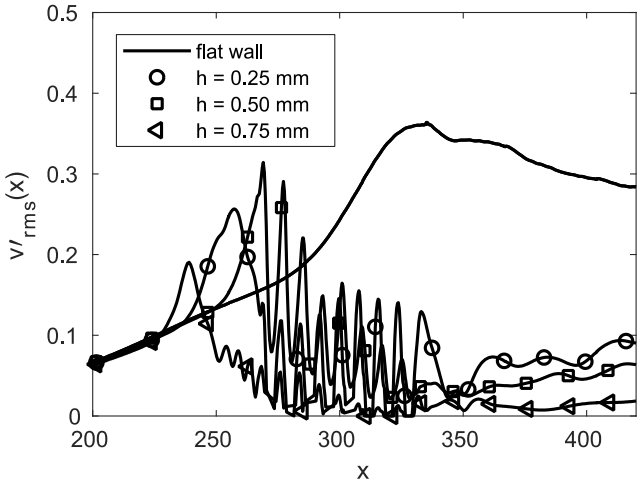

Figure 30d)

Root mean square of the wall-normal velocity distribution along the wall (y = 0.7): a) hump; b) dip; c) sine 1; d) sine 2.

CHAPTER VI

CONCLUSIONS

The effect of various two-dimensional surface deformations on disturbance propagating inside a high-speed boundary layer was analyzed in this thesis with the assistance of direct numerical simulations. The two types of disturbances analyzed were: a localized wall pulse in the wall-normal velocity direction and a periodic wall blowing and suction. Both disturbances were imposed within the wall boundary condition. The 2-D wall deformations that were examined were: backward step, forward steps, combinations of a forward and backward steps, surface dip, surface hump, and two types of wavy surfaces consisting of successive dips or successive humps. A study in terms of varying the streamwise width of the deformations and varying the height of the deformations was conducted. A grid study for the flat wall case was conducted to decide on the proper grid density, that would allow for accurate results and not waste computational resources. Based on the data from the linearized stability analysis of the flat wall case, the location of the synchronization point was calculated and the wall deformations were placed downstream of the synchronization point.

The results show that the wall deformations had a stabilizing effect on the imposed disturbances, especially the deformations that feature an adverse pressure gradient in the upstream followed by a favorable pressure gradient or a succession of adverse and favorable pressure gradients. The effectiveness of reducing the disturbance

amplitude varied with each of the wall deformations analyzed in this study. The various pressure disturbance contour plots and line plots of root mean square of the wall-normal velocity and root mean square density disturbances displayed that the combination of the forward-backward steps, sine 2 and the forward step cases were the most effective in reducing the amplitudes of the two types of disturbances utilized in this study. The combination of the backward-forward steps and the surface dip cases were the least effective in reducing the amplitudes of both types of disturbances, when compared to the flat wall case. A possible explanation for the mechanism of energy reduction was proposed: part of the energy from the disturbance is deviated outside of the boundary layer by the mean flow discontinuity that is generated by the presence of the wall deformation; this becomes more significant when there is an adverse pressure gradient present in the upstream of the deformation. However, because the portion of the deviated energy was found to be small, it was concluded that this mechanism does not have a significant effect.

It was observed that the variation of the streamwise width of the wall deformation, with the height remaining constant, plays an important role in the reduction of the disturbance energy. In Fong et al.[16,17] the variation of the roughness height and the location of the roughness with respect to the synchronization point was analyzed. When the streamwise width of the hump and dip cases was increased, the reduction of the disturbance amplitude was not as significant, especially for the periodic disturbance. This result contrasts the results presented in Fong et al.[17], but it is necessary to mention that this reduction is only valid for a continuous roughness element, while the non-continuous roughness elements, such as the combination of a forward and backward

steps, there is no significant difference in reduction when varying the streamwise width. For the combination of a backward and forward steps, as the length of separation between the two steps is increased, the reduction of the disturbance energy is increased. For the combination of a forward and then backward step case, as the separation length is varied, it does not alter the reduction in the disturbance energy because the forward step is located upstream of the backward step had the most significant impact on the disturbances.

When varying the height of the wall deformations, some of the results coincided with the results presented in Fong et al.[15-17], while a few cases had non-conclusive results. The wall deformation cases that have a protuberance above the flat wall and the backward step case had conclusive results, in that the reduction in disturbance energy increased as the deformation height was increased and vice versa. For the combination of a backward and forward step, dip and sine 1 cases, the results are not conclusive, since altering the deformation height from the original height of 0.5mm caused a reduction in the disturbance energy greater than the original height.

FUTURE WORK

Some future work to consider after reviewing the study performed in this paper, is to further analyze the variation in step height for the wall deformation cases that have a deformation located below the wall line. Perform parabolic stability analysis on the wall deformation cases present in this study to locate the synchronization point of the first and second modes downstream of the wall deformations, to further analyze the effectiveness of the deformations on the stability of the high-speed boundary layer flow.

REFERENCES

[1] Gregory, N., Walker, W. S., and Johnson (1951) Part I: The effect on transition of isolated excrescences in the boundary layer; Part II: Brief flight tests on a Vampire I aircraft to determine the effect of isolated surface pimples on transition, *Reports and Memoranda 2779*, Aeronautical Research Council.

[2] Drake, A. and Bender, A. (2009) Surface excrescence transition study, *Technical Report AFRL-RB-WP-TR-2009-3109*, Wright-Patterson AFB, OH.

[3] Duncan, Crawford, B., Tufts, M.W., Saric, W.S. and Reed, H.L. (2013) Effects of Step Excrescences on Swept-Wing Transition, *AIAA Paper* 2013-2412.

[4] Choudhari, M. and Fischer, P. (2005) Roughness induced Transient Growth, *AIAA Paper* 2005-4765.

[5] Yoon, S., Barnhardt, M. and Candler, G.V. (2010) Simulations of high-speed flows over an isolated roughness, *AIAA Paper* 2010-1573.

[6] Muppidi, S. and Mahesh, K. (2012) Direct numerical simulations of roughness-induced transition in supersonic boundary layers, *Journal of Fluid Mechanics*, Vol. 693, pp. 288-56.

[7] Iyer, P.S., Muppidi, S. and Mahesh, K. (2012) Boundary layer transition in high-speed flows due to roughness, *AIAA Paper* 2012-1106.

[8] Brehm, C., Koevary, C., Dackermann, T. and Fasel H.F. (2011) Numerical Investigation of the Influence of Distributed Roughness on Blasius Boundary Layer Stability, *AIAA Paper* 2011-563.

[9] Duan, L. and Choudhari, M. (2012) Effects of Riblets on Skin Friction in High-Speed Turbulent Boundary Layers, *AIAA Paper* 2012-1108.

[10] Subbareddy, P.K., Bartkowitcz, M. and Candler, C.V. (2012) Numerical simulations of roughness induced instabilities in the Purdue Mach 6 Tunnel, *Journal of Fluid Mechanics*, Vol. 748, pp. 848-878.

[11] Rizzetta, D. P. and Visbal, M. R. (2014) Numerical Simulation of Excrescence Generated Transition, *AIAA Journal*, Vol. 52, pp. 385-397

[12] Sescu, A., Visbal and Rizzetta, D. (2014) Numerical Study of Boundary Layer Receptivity to Free-stream Disturbances and Surface Excrescences, *AIAA Paper*.

[13] Sescu, A., Visbal, M. and Rizzetta, D. (2015) A Study of the Effect of Surface Excrescences and Free-stream Disturbances on Boundary Layers, *International Journal for Numerical Methods in Fluids*, Vol. 77, pp. 509-525.

[14] Chaudhry, R.S., Subbareddy, P.K., Nompelis, I. and Candler, G.V. (2015) Direct numerical simulation of roughness induced transition in the VKI Mach 6 Tunnel, *AIAA Paper* 2015-0274.

[15] Fong, K., Wang, X., and Zhong, X. (2013) Stabilization of Hypersonic Boundary Layer by 2-D Surface Roughness, *AIAA Paper* 2013-2985.

[16] Fong, K., Wang, X., and Zhong, X. (2014) Numerical simulation of roughness effect on the stability of a hypersonic boundary layer, *Computers & Fluids*, Vol. 96, pp. 350-367.

[17] Fong, K., Wang, X., and Zhong, X. (2015) Parametric Study on Stabilization of Hypersonic Boundary-Layer Waves Using 2-D Surface Roughness, *AIAA Paper* 2015-08

[18] Fong, K., Wang, X., Huang, Y., Zhong, X., McKiernan, G., Fisher, R., and Schneider, S. (2015) Second Mode Suppression in Hypersonic Boundary Layer by Roughness: Design and Experiments, *AIAA Journal*, Vol 53 , pp. 3138-3144

[19] Duan, L., Wang, X., and Zhong, X. (2013) Stabilization of a Mach 5.92 Boundary Layer by Two-Dimensional Finite-Height Roughness, *AIAA Journal*, Vol. 51, pp. 266-270

[20] Park, D. and Park, S.O. (2016) Study of effect of a smooth bump on hypersonic boundary layer instability, *Theoretical and Computational Fluid Dynamics*, May 2016, pp. 1-21.

[21] Bountin, D., Chimitov, T., Maslov, A., Novikov, A., Egorov, I., Fedorov, A. and Utyuzhnikov, S. (2013) Stabilization of a hypersonic boundary layer using a wavy surface, *AIAA Journal*, Vol. 51, pp. 1203-1210.

[22] Mortensen, C.H. and Zhong, X. (2015) Numerical Simulation of Hypersonic Boundary-Layer Instability in a Real Gas with Two-Dimensional Surface Roughness, *AIAA Paper* 2015-3077.

[23] Schneider, P. (2008) Effects of Roughness on Hypersonic Boundary-Layer Transition, *Journal of Spacecraft and Rockets*, Vol. 45.

[24] Mack, L. M. (1975) On the application of linear stability theory and the problem of supersonic boundary-layer transition, *AIAA Journal*, Vol. 13.

[25] Gaponov, S. A. (1993) Excitation of Instability Waves in the Supersonic Boundary Layer by Sound, IUTAM Symposium Potsdam, Springer-Verlag.

[26] Gaponov, S. A. and Smorodsky, B. V. (1999) Supersonic Boundary Layer Receptivity to Streamwise Acoustic Field, IUTAM Symposium, Spinger-Verlag.

[27] Fedorov, A. V., and Khokhlov, A. P. (1991) Excitation of Unstable Modes in a Supersonic Boundary Layer by Acoustic Waves, *Fluid Dynamics*, No. 9, pp. 456-467.

[28] Fedorov, A. V., and Khokhlov, A. P. (1992) Sensitivity of a Supersonic Boundary Layer to Acoustic Disturbances, *Fluid Dynamics*, No. 27, pp. 29-34.

[29] Sakaue, S., Asia, M., and Nishioka, M. (2000) On the Receptivity process of supersonic laminar boundary layer, Laminar Turbulent Transition, Heidelberg, Springer-Verlag

[30] Fedorov, A. V. (2002) Receptivity of High Speed Boundary Layer to Acoustic Disturbances, *AIAA Paper* 2002-2846.

[31] Balakumar, P. (2003) Transition in a Supersonic Boundary layer Due to Roughness and Acoustic Disturbances, *AIAA Paper* 2003-3589.

[32] Balakumar, P. (2005) Transition in a Supersonic Boundary layer Due to Acoustic Disturbances, *AIAA Paper* 2005-0096.

[33] Balakumar, P. (2009) Receptivity of a supersonic boundary layer to acoustic disturbances, *AIAA Journal*, Vol. 47, pp. 1069-178.

[34] Holloway, P. and Sterrett, J., Effect of Controlled Surface Roughness on Boundary-Layer Transition and Heat Transfer at Mach Numbers of 4.8 and 6.0, TN-D-2054, NASA.

[35] Malik, M. R. (1990) Numerical Methods for Hypersonic Boundary Layer Stability, *Journal of Computational Physics*, Vol. 86, pp. 376-413.

[36] Zhou, Y., Liu, W., Chai, Z. and Yang, X. (2017) Numerical simulation of wavy surface effect on the stability of a hypersonic boundary layer, *Acta Astronautica*, Vol. 140, pp. 485-496.

[37] Liu. X., Osher, S. and Chan, T. (1994) Weighted essentially non-oscillatory schemes, *Journal of Computational Physics*, Vol. 115, pp. 200-212.

[38] Tam, C.K.W. and Webb, J.C. (1993), Dispersion-relation-preserving finite difference schemes for Computational Aeroacoustics, *Journal of Computational Physics*, Vol. 107, pp. 262-281.

[39] Bogey, C., Bailly, C. (2004), A family of low dispersive and low dissipative explicit schemes for flow and noise computation, *Journal of Computational Physics*, Vol. 194, pp. 194-214.

[40] Kennedy, C.A. and Carpenter, M.H. (1997), Comparison of several numerical methods for simulation of compressible shear layers, *NASA Technical Report*, NASA-97-TP3484.

[41] Kim, J.W. and Lee, D.J. (2000) Generalized Characteristic Boundary Conditions for Computational Aeroacoustics, *AIAA Journal*, Vol. 38, pp. 2040-2049.

[42] Bogey, C., Bailly, C., and Juve, D. (2002), A shock-capturing methodology based on adaptative spatial filtering for high-order non-linear computations, *Journal of Computational Physics*, Vol. 228, pp. 1447-1465.

[43] Sawaya, J., Sassanis, V., Yassir, S., Sescu, A. and Visbal, M. (2018) Assessment of the impact of two-dimensional wall deformations' shape on high-speed boundary layer disturbances, *AIAA Paper*.